

Note: This work has not yet been peer-reviewed and is provided by the contributing author(s) via EarthArXiv.org as a means to ensure timely dissemination of scholarly and technical work on a noncommercial basis. Copyright and all rights therein are maintained by the author(s) or by other copyright owners. It is understood that all persons copying this information will adhere to the terms and constraints invoked by each author's copyright. This work may not be reposted without explicit permission of the copyright owner.

This work is under review at the *Journal of Physical Oceanography*. Copyright in this work may be transferred without further notice.

Abyssal Circulation Driven By Near-Boundary Mixing:

Water Mass Transformations and Interior Stratification

Henri F. Drake*

*MIT-WHOI Joint Program in Oceanography/Applied Ocean Science & Engineering, Cambridge
and Woods Hole, Massachusetts.*

Raffaele Ferrari

Massachusetts Institute of Technology, Cambridge, Massachusetts.

9

Jörn Callies

10

California Institute of Technology, Pasadena, California.

11 **Corresponding author address:* Henri F. Drake, Department of Earth, Atmospheric, and Planetary
12 Sciences, Massachusetts Institute of Technology, 77 Massachusetts Ave, Cambridge, MA 02139.
13 E-mail: henrifdrake@gmail.com

ABSTRACT

14 The emerging view of the abyssal circulation is that it is associated with
15 bottom-enhanced mixing, which results in downwelling in the stratified ocean
16 interior and upwelling in a bottom boundary layer along the insulating and
17 sloping seafloor. In the limit of slowly-varying vertical stratification and to-
18 pography, however, boundary layer theory predicts that these up- and down-
19 slope flows largely compensate, such that net watermass transformations
20 along the slope are vanishingly small. Using a Planetary-Geostrophic Cir-
21 culation Model that resolves both the boundary-layer dynamics and the large-
22 scale overturning in an idealized basin with bottom-enhanced mixing along a
23 mid-ocean ridge, we show that vertical variations in stratification become suf-
24 ficiently large at equilibrium to reduce the degree of compensation along the
25 mid-ocean ridge flanks. The resulting large net transformations are similar to
26 estimates for the abyssal ocean and span the vertical extent of the ridge. These
27 results suggest that boundary flows generated by mixing play a crucial role in
28 setting the global ocean stratification and overturning circulation, requiring a
29 revision of abyssal ocean theories.

30 **1. Motivation**

31 The abyssal ocean, below 2500 m, is a massive reservoir for climatically active tracers such
32 as carbon and heat. The rates at which heat is mixed and advected into the high capacity abyssal
33 ocean are key parameters in understanding both past climate reconstructions (e.g. Toggweiler et al.
34 1989) and future projections of climate change (e.g. Hansen et al. 1985). Similarly, the partitioning
35 of carbon between the deep ocean and the atmosphere is a major factor on millennial-scale climate
36 change, whether natural (e.g. Sarmiento and Toggweiler 1984) or anthropogenic in origin (Archer
37 et al. 1998). It is thus vital to have a firm phenomenological and dynamical understanding of the
38 abyssal ocean's mean state.

39 The general structure of the abyssal ocean circulation is easily inferred from surface buoyancy
40 fluxes and large-scale tracer properties (Sverdrup et al. 1942). Antarctic Bottom Waters, the dens-
41 est oceanic waters, form in the Southern Ocean and fill the global abyssal oceans up to a depth of
42 about 2500 m (Talley 2013a). They outcrop at the surface only in the Southern Ocean, where they
43 experience a significant area-integrated buoyancy loss (Abernathey et al. 2016) and are converted
44 back into lighter waters by mixing with lighter overlying waters, resulting in a diabatic abyssal
45 overturning circulation of $O(15 \text{ Sv})$, where $1 \text{ Sv} = 10^6 \text{ m}^3 \text{ s}^{-1}$. Non-linearities in the equation
46 of state of seawater and geothermal heating at the seafloor are thought to play secondary roles
47 in shaping this circulation (Emile-Geay and Madec 2009; de Lavergne et al. 2016a) and will be
48 ignored in the conceptual models described below.

49 Classical theories for the abyssal ocean describe the steady state circulation and stratification of
50 a flat-bottom ocean forced by uniform turbulent mixing (Stommel 1957; Robinson and Stommel
51 1959; Stommel and Arons 1959b,a; Munk 1966). These theories remain pedagogically useful,
52 but are at best qualitative descriptions, as demonstrated for example by the fact that the direction

53 of the flow in the Stommel and Arons (1959b) solution changes sign when a sloping seafloor is
54 introduced (Rhines 1993) and that the Munk (1966) solution does not satisfy the no-flux bound-
55 ary condition at the seafloor. The classical view of a uniform mixing-driven upwelling is further
56 challenged by the observation that turbulent mixing is typically bottom-enhanced over rough to-
57 pography (see MacKinnon et al. 2017 for a recent review), reversing the sign of the vertical flow
58 implied by the interior ocean vertical density balance (Polzin et al. 1997; Ferrari et al. 2016).

59 Since Munk (1966), several approaches have been taken to address the limitations of classical
60 theories. First, boundary layer theories (Wunsch 1970; Thorpe 1987; Garrett 1990; Thompson
61 and Johnson 1996) arose to elucidate the local behavior of mixing-induced flow along a sloping
62 and insulating sea floor. Second, the limitations of the Stommel and Arons (1959b) theory in-
63 spired a number of extensions to account for baroclinic structure (Kawase 1987; Pedlosky 1992),
64 non-uniform seafloor depth (Rhines 1993), and/or non-uniform turbulent diffusivities κ (Marotzke
65 1997; Samelson 1998). Third, the observation of bottom-enhanced mixing motivated the devel-
66 opment of progressively more sophisticated parameterizations of vertical (or diapycnal) turbu-
67 lent diffusivities (Bryan and Lewis 1979; St. Laurent and Garrett 2002; Polzin 2009) which have
68 been subsequently implemented into general circulation models (Huang and Jin 2002; Jayne 2009;
69 Melet et al. 2016). Fourth, the conundrum of interior downwelling implied by bottom-enhanced
70 mixing was resolved by applying the watermass transformation framework to a downwelling in-
71 terior layer of turbulent buoyancy flux divergence and an upwelling bottom boundary layer of
72 turbulent buoyancy flux convergence, respectively (Ferrari et al. 2016; de Lavergne et al. 2016b;
73 McDougall and Ferrari 2017). Despite the direct relevance of all of these approaches to the abyssal
74 circulation, there has been little work done to unify them into a general theory of the abyssal cir-
75 culation and stratification.

76 Building on the framework introduced by Callies and Ferrari (2018) (hereafter, CF18), we
77 present a unified prognostic model of the circulation in an abyssal basin forced by bottom-
78 enhanced mixing along a mid-ocean ridge. We modify the geometry, buoyancy forcing, and initial
79 condition of the CF18 model to include the effects of a smooth mid-ocean ridge (with the effects
80 of local roughness parameterized by bottom-enhanced mixing) and of a non-uniform background
81 stratification on the circulation. Our approach is to formulate the simplest possible model which
82 captures what we believe to be the key aspects of the problem: 1) the transformation of abyssal
83 bottom waters into relatively lighter deep waters by bottom-enhanced mixing on the flanks of a
84 mid-ocean ridge, 2) frictional processes acting on boundary currents, 3) restratification of abyssal
85 mixing layers by baroclinic turbulence (crudely parameterized as a linear drag on the horizontal
86 flow), and 4) bottom water formation in the Southern Ocean.

87 The general structure of the abyssal circulation that emerges from the model consists of layered
88 deep western boundary currents along the western continental slope which are connected by zonal
89 flows to watermass transformations driven by bottom-enhanced mixing along a mid-ocean ridge,
90 as schematized in Figure 1. The evolution of the interior stratification and the mixing layer wa-
91 termass transformations are coupled by slope-normal exchange flows, with the vertically-varying
92 equilibrium stratification being determined by a combination of the mixing layer dynamics and the
93 formation of dense waters in the south. Finite net watermass transformations arise ubiquitously
94 along the flanks of the mid-ocean ridge, supported by vertical variations in the interior stratifi-
95 cation, such that the crest of the mid-ocean ridge determines the vertical extent of the abyssal
96 overturning cell, in contrast to a previous constant-stratification interpretation in which finite net
97 transformations are confined to the base of topographic slopes (CF18).

98 The paper is structured as follows. Section 2 reviews the results of several theories of abyssal
99 stratification and circulation in the literature. Section 3 presents the formulation of the Planetary

100 Geostrophic Circulation Model (PGCM) used to produce the simulation results presented in the
101 paper. Section 4 describes the general structure of the abyssal circulation as it emerges in the
102 PGCM. In Section 5 we use local solutions to the one-dimensional boundary layer equations to
103 emulate the three-dimensional abyssal circulation in the PGCM. Section 6 describes the spin-up to
104 equilibrium of the vertical structure of abyssal interior stratification and its influence on watermass
105 transformations. Section 7 compares watermass transformations in our PGCM simulations with
106 estimates for the mid-ocean ridges of the Pacific, Atlantic, and Indian Ocean basins. Section 8
107 compares diagnostic estimates of abyssal upwelling from the watermass transformation framework
108 with the classic vertical advection-diffusion framework and evaluates the relative contributions of
109 various physical terms of the watermass transformation. Section 9 discusses the implications of
110 our results, some key caveats, and some promising future directions.

111 **2. Theoretical Background**

112 *a. Classical theories of abyssal stratification and circulation*

113 Modern theories of the abyssal circulation begin with a series of papers by Stommel and Arons
114 (1959b,a). In their theory, the circulation of a homogeneous abyssal layer is fed by high-latitude
115 sources of abyssal water (diabatic downwelling) and driven by a uniformly-distributed sink (di-
116 abatic upwelling) of abyssal water. A uniform upwelling across the base of the thermocline is
117 prescribed, inspired by the thermocline-thermohaline theory of Robinson and Stommel (1959).
118 Munk (1966) further simplifies the Robinson and Stommel (1959) balance by restricting his atten-
119 tion to the deep ocean (i.e. below the thermocline) and by considering only vertical advection and
120 diffusion,

$$u^z \partial_z b = \partial_z (\kappa \partial_z b), \quad (1)$$

121 where b is buoyancy, u^z is a uniform vertical velocity, κ is a uniform turbulent diffusivity. The
 122 Munk formulation allows exponential solutions which can be fit to the observed temperature pro-
 123 files and combined with fits of an advection-diffusion-decay equation to radiocarbon profiles to
 124 yield the canonical estimate of deep ocean mixing $\kappa \simeq 10^{-4} \text{ m}^2\text{s}^{-1}$ for a uniform upwelling of
 125 $u^z = 1.4 \times 10^{-7} \text{ m/s}$.

126 The horizontal abyssal circulation associated with the upwelling is described by Stommel and
 127 Arons (1959b,a): interior flow is geostrophically-balanced and its meridional component u^y is
 128 driven by vortex stretching, as shown by the vertically-integrated planetary-geostrophic vorticity
 129 balance

$$\beta U^y = f \frac{u_0^z}{H}, \quad (2)$$

130 where H is the thickness of the abyssal layer, $u_0^z > 0$ is the upwelling across the base of the
 131 thermocline, f is the Coriolis parameter, $\beta > 0$ is the meridional gradient of the Coriolis parameter,
 132 and the vertically-integrated flow U^y is thus poleward in both hemispheres (see Pedlosky 1996
 133 for an elucidating derivation). Inspired by the success of analogous theories for the wind-driven
 134 gyre circulation (Stommel 1948), Stommel and Arons (1959b,a) suppose the existence of a deep
 135 western boundary current in which frictional effects allow the current to deviate from geostrophy
 136 and return the interior flow such that the abyss conserves mass.

137 *b. Turning ocean mixing upside down*

138 The Stommel and Arons (1959b,a) and Munk (1966) theories rely on the existence of a uniform
 139 turbulent diffusivity $\kappa \simeq 10^{-4} \text{ m}^2\text{s}^{-1}$, roughly an order of magnitude larger than the interior ocean
 140 mixing inferred from observations (Gregg 1989; Ledwell et al. 1993). While sufficiently vigorous
 141 mixing was eventually discovered deeper in the ocean near rough seafloor topography (Polzin
 142 et al. 1997; Ledwell et al. 2000; Sheen et al. 2013), the abyssal mixing problem only became

143 more complicated: applying the vertical advection-diffusion balance (eq.1) point-wise to mixing
 144 profiles $\kappa(z)\partial_z b$ that increase with depth implies diapycnal *downwelling*

$$u^z = (\partial_z b)^{-1} \partial_z (\kappa \partial_z b) < 0, \quad (3)$$

145 in contrast to the diapycnal *upwelling* required to balance diapycnal downwelling at high lati-
 146 tudes¹!

147 This apparent conundrum is resolved by considering the insulating boundary condition at a
 148 sloping seafloor, which causes buoyancy convergence and hence diapycnal upwelling in a thin
 149 bottom boundary layer (Polzin et al. 1997; Ferrari et al. 2016; de Lavergne et al. 2016b). In this
 150 framework, the abyssal overturning is the net effect of downwelling driven by bottom-enhanced
 151 mixing in a stratified mixing layer and upwelling driven by buoyancy convergence in a bottom
 152 boundary layer, which we collectively refer to as abyssal mixing layers (CF18).

153 *c. A puzzling constraint from boundary layer theory*

154 Bottom boundary layer theory (see review of Garrett et al. 1993) is a useful dynamical approach
 155 to the problem of flow driven by near-boundary mixing on a slope, which exerts a strong control on
 156 the basin-scale abyssal circulation (CF18). Following Thorpe (1987), who built on the approaches
 157 of Wunsch (1970) and Phillips (1970), we rotate the Boussinesq equations into slope coordinates
 158 and assume the flow depends only on the slope-normal coordinate z' , which gives the simplified
 159 buoyancy equation (see derivation of full equation set in Section 5a):

$$\partial_t b' + u^{x'} N_0^2 \sin \theta = \partial_{z'} [\kappa (N_0^2 \cos \theta + \partial_{z'} b')] \quad (4)$$

160 where $u^{x'}$ is the up-slope velocity, θ the slope angle, $\kappa = \kappa(z')$ the turbulent diffusivity, and we
 161 decompose the buoyancy field $b(x, y, z, t) = N_0^2 z + b'(x, y, z, t)$ into a background corresponding to

¹While the sign of the vertical velocity changes, we note that $\partial_z u^z > 0$ and thus the interior geostrophic flow driven by vortex stretching is still of the same sign as in the Stommel-Arons solution.

162 a constant stratification N_0^2 and a buoyancy anomaly $b' = b'(z')$. The boundary conditions are a no-
 163 flux condition $\partial_{z'} b = \partial_{z'} b' + N_0^2 \cos \theta = 0$ at the seafloor $z' = 0$ and decay conditions $\partial_{z'} u^{x'}, \partial_{z'} b' \rightarrow 0$
 164 as $z' \rightarrow \infty$. At steady state, the boundary layer equation for the buoyancy anomaly (eq. 4) can be
 165 integrated from $z' = 0$ to $z' \rightarrow \infty$, which yields

$$\Psi_{\text{bg}} \equiv \kappa_{\text{bg}} \cot \theta \quad (5)$$

166 for the net up-slope transport per unit length $\Psi_{\text{bg}} = \int_0^\infty u^{x'} dz'$, where $\kappa_{\text{bg}} \equiv \kappa(z \rightarrow \infty)$ is the
 167 background diffusivity. The simplicity of this integral constraint is surprising: the net up-slope
 168 transport depends only on the background turbulent diffusivity κ_{bg} and the slope angle θ , and is
 169 independent of other environmental parameters which might be expected to influence diapycnal
 170 transport, such as frictional parameters, the background stratification N_0^2 , the Coriolis parameter
 171 f , and the vertical structure of the turbulent diffusivity $\kappa(z)$.

172 Integrating the prediction Ψ_{bg} for the diapycnal transport per unit length along the perimeter
 173 $L_{\text{global}} \simeq 10^8$ m of the global mid-ocean ridge system (Callies 2018) for a typical ridge slope
 174 $\tan(\theta) = 2 \times 10^{-3}$ and a background diffusivity of $\kappa_{\text{bg}} \simeq 10^{-5} \text{ m}^2\text{s}^{-1}$ produces a global mixing-
 175 driven diapycnal overturning transport of $L_{\text{global}} \kappa_{\text{bg}} \cot \theta \simeq 0.5$ Sv, more than an order of magni-
 176 tude smaller than the observed abyssal diapycnal overturning transport of roughly 15 Sv (Lumpkin
 177 and Speer 2007).

178 CF18 resolve this conundrum by using the magnitude of the upwelling-downwelling ‘dipole’
 179 from boundary layer theory as a prediction for the net watermass transformation, since at the
 180 base of topographic slopes the flows in and out of the boundary layers occur at different density
 181 classes and thus drive a diabatic overturning. They find that the strictly upwelling transport in the
 182 bottom boundary layer accurately predicts the scaling of the maximum net diapycnal overturning

183 transport, although the predicted overturning is unrealistically confined to the base of topographic
184 slopes, where the constraints from one-dimensional boundary layer theory break down.

185 *d. Boundary-interior exchange*

186 The integral constraint $\Psi_{\text{bg}} \equiv \kappa_{\text{bg}} \cot \theta$ (eq. 5) relies on the assumption of constant background
187 stratification N_0^2 and slope angle θ . By construction, none of the other terms are assumed to vary in
188 the plane of the slope (x', y') either; it follows that there are no cross-slope convergences $\partial_{x'} u^{x'} = 0$
189 and hence no slope-normal exchange between the abyssal mixing layers and the interior, $u^{z'} = 0$
190 (Wunsch 1970).

191 With a vertically varying stratification $N^2(z)$, however, variations in the buoyancy gradient
192 project onto the cross-slope direction $x' = x \cos \theta + z \sin \theta$, introducing a second dimension to the
193 problem (e.g. Phillips et al. 1986; Salmun et al. 1991) and permitting both slope-normal exchange
194 flows $u^{z'} \neq 0$ and a net diapycnal transport $\Psi_{\infty} \equiv \int_0^{\infty} u^{x'} dz' \neq \Psi_{\text{bg}}$. Heterogeneities can also arise
195 due to cross-slope variations in the turbulent diffusivity $\kappa(x, y)$ or the slope angle $\theta(x, y)$ (Dell and
196 Pratt 2015), and have been argued to contribute significantly to oceanic watermass transformations
197 (McDougall and Ferrari 2017; de Lavergne et al. 2017; Holmes et al. 2018). These additional het-
198 erogeneities are both kept relatively small by construction in our idealized model configuration to
199 keep the focus on the effects of variations in the basin stratification.

200 *e. Dynamics controlling the interior abyssal stratification*

201 The abyssal stratification is thought to be controlled by the combined effects of 1) diapycnal mix-
202 ing in ocean basins and 2) the competing effects of winds and mesoscale eddies in setting the slope
203 of isopycnals in the Southern Ocean. Diapycnal mixing maintains the stable stratification of the
204 abyssal ocean by effectively diffusing buoyancy downwards, transforming dense abyssal waters

205 into lighter deep waters (Munk 1966). This vertical advection-diffusion model is an incomplete
206 model of the abyssal stratification, however, as it omits the complementary process which closes
207 the overturning circulation by transforming light deep waters into denser abyssal waters. Munk
208 and Wunsch (1998) consider a heuristic correction to Munk (1966)'s vertical advection-diffusion
209 equation for the effect of horizontal advection from regions of high mixing (or homogenization
210 by convection), which acts to restratify regions of weak mixing. A breakthrough in understanding
211 the abyssal stratification was the development of quasi-adiabatic theories of Southern Ocean cir-
212 culation. In these theories, deep waters are upwelled adiabatically along sloping isopycnals in the
213 Southern Ocean, are transformed into abyssal waters in the Southern Ocean mixed layer by a neg-
214 ative surface buoyancy flux, and return to the abyss adiabatically along isopycnals (Marshall and
215 Speer 2012, and references therein). The Southern Ocean isopycnal slope is determined by a bal-
216 ance between wind stress and stirring by mesoscale eddies, which steepen and flatten isopycnals,
217 respectively (Marshall and Radko 2003).

218 Building on these two independent theories, Nikurashin and Vallis (2011) develop an idealized
219 model which couples quasi-adiabatic Southern Ocean dynamics to a diabatic abyssal ocean basin
220 and predicts the abyssal stratification and circulation, given only surface boundary conditions and
221 mixing coefficients. For moderate diapycnal mixing of $10^{-5} \text{ m}^2\text{s}^{-1} < \kappa < 10^{-3} \text{ m}^2\text{s}^{-1}$, a regime
222 applicable to both the Ocean and the model described here, the Nikurashin and Vallis (2011) model
223 predicts that the interior abyssal stratification depends both on winds and eddies in the Southern
224 Ocean and diapycnal mixing in the basin.

225 A promising aspect of zonally-integrated models of the meridional overturning circulation (e.g
226 Nikurashin et al. 2012; Thompson et al. 2016) is that they accurately reproduce the overturning
227 and stratification exhibited by idealized “box”-geometry general circulation models. The emerging
228 view, however, is that the abyssal circulation of the ocean is controlled by mixing layer flows

229 along sloping boundaries and thus that the commonly-used “box” geometry models may be a
 230 misleading point of reference for theories of the abyssal stratification and circulation (Ferrari et al.
 231 2016). Building on CF18, we describe the formulation of an improved idealized general circulation
 232 model in a “bowl + ridge” geometry which accommodates the recent revisions to our theoretical
 233 understanding of the abyssal ocean circulation.

234 **3. Planetary Geostrophic Circulation Model (PGCM)**

235 The numerical model used here is the Planetary Geostrophic Circulation Model (PGCM) devel-
 236 oped by CF18 to study how bottom-enhanced mixing on slopes drives an abyssal circulation. We
 237 describe the key elements of our PGCM configuration below, which closely follows the exposi-
 238 tion of CF18. The main differences between the present study and CF18 are the inclusion of the
 239 mid-ocean ridge, the localization of vigorous bottom-enhanced mixing to a mid-ocean ridge, and
 240 the generalization to vertically-varying interior stratifications. Readers familiar with the methods
 241 of CF18 can skip Section 3 and simply consult Figure 2, which summarizes our changes to the
 242 configuration.

243 *a. Equations*

244 The model solves the Navier-Stokes equations under the Boussinesq and planetary-scale
 245 geostrophic approximations, with parameterizations for the frictional and diabatic effects of unre-
 246 solved processes, given by

$$f\mathbf{z} \times \mathbf{u} = -\nabla p + b\mathbf{z} - r(u^x\mathbf{x} + u^y\mathbf{y}), \quad (6)$$

$$\nabla \cdot \mathbf{u} = 0, \text{ and} \quad (7)$$

$$\frac{\partial b}{\partial t} + \mathbf{u} \cdot \nabla b = \nabla \cdot (\kappa \nabla b) - \lambda(y)(b - B(z)), \quad (8)$$

247 where t is time; $\mathbf{x}, \mathbf{y}, \mathbf{z}$ are unit vectors pointing east, north, and up, respectively; $f = \beta y$ is the lin-
248 earized Coriolis parameter (β -plane approximation); $\mathbf{u} = (u^x, u^y, u^z)$ is the velocity vector; p is the
249 pressure divided by a reference density; b is the buoyancy; r is a frictional parameter; $\kappa = \kappa(x, y, z)$
250 is a spatially-dependent turbulent diffusivity; and $\lambda = \lambda(y)$ is a meridionally-varying restoring rate
251 (see Section 3c). The system of equations (6) - (8), with appropriate initial and boundary condi-
252 tions, yields a self-consistent and prognostic model of abyssal circulation and stratification.

253 The Boussinesq approximation filters out acoustic waves while the planetary-geostrophic ap-
254 proximation filters out gravity waves and geostrophic turbulence. The resulting planetary-
255 geostrophic equations are appropriate for basin-scale oceanic circulations and are typically used
256 for idealized studies of the abyssal circulation (e.g Pedlosky 1996, and references therein) and
257 intermediate-complexity earth system models (e.g. Holden et al. 2016). While it is computation-
258 ally and conceptually useful that the planetary-geostrophic equations filter out the effects of fast
259 waves and turbulence, the turbulent fluxes of these relatively small-scale flows are thought to
260 have leading order effects on abyssal mixing layers. We include their qualitative effects in the
261 planetary-geostrophic formulation by way of two idealized parameterizations.

262 First, to include the effects of turbulent mixing produced by the local breaking of internal waves
263 generated by flow over rough topography, we introduce a term for the turbulent buoyancy flux
264 convergence $\nabla \cdot (\kappa \nabla b)$ to the buoyancy equation (e.g. as in St. Laurent and Garrett 2002). The
265 imposed spatially-dependent turbulent diffusivity $\kappa(x, y, z)$ approximates the leading-order spatial
266 structure described by observational estimates² (e.g. Polzin et al. 1997; Waterhouse et al. 2014)
267 and is described in detail in Section 3c.

²Quantitatively similar profiles of turbulent kinetic energy dissipation are reproduced in simulations of internal wave turbulence above rough topography, wherein energy from a geostrophic mean flow (Nikurashin and Ferrari 2009) or the barotropic tide (Nikurashin and Legg 2011) is converted into unstable high-mode internal waves via a cascade of wave-wave interactions.

268 Second, to include the qualitative effects of isopycnal mixing by baroclinic turbulence in re-
 269 stratifying the abyssal mixing layers (Callies 2018) and in thickening western boundary currents
 270 (e.g. Stommel 1948), we introduce a dissipative term to the momentum equation. Greatbatch
 271 and Lamb (1990) show that introducing vertical momentum diffusion $\partial_z (v_{\text{eddy}} \partial_z \mathbf{u})$ to the plane-
 272 tary geostrophic equations with an eddy viscosity $v_{\text{eddy}} = \kappa_{\text{GM}} f^2 / N^2$ is equivalent to introducing
 273 isopycnal diffusion of potential vorticity with an effective isopycnal diffusivity of κ_{GM} (Gent and
 274 McWilliams 1990). Following Salmon (1992), we simplify the dynamics further by using a linear
 275 friction term (Rayleigh drag), $-r(u^x \mathbf{x} + u^y \mathbf{y})$ and scale the frictional parameter r according to the
 276 Greatbatch and Lamb (1990) parameterization,

$$r = \kappa_{\text{GM}} \frac{f^2}{\delta^2 N^2} \approx 1.2 \times 10^{-5} \text{ s}^{-1}, \quad (9)$$

277 where we choose $\delta = 400$ m to be roughly the thickness of the abyssal mixing layers observed in
 278 the Brazil Basin (Callies 2018); typical abyssal mixing layer values of $f = 5 \times 10^{-5} \text{ s}^{-1}$ and $N^2 =$
 279 $5 \times 10^{-7} \text{ s}^{-1}$; and in the absence of observational or theoretical constraints assume $\kappa_{\text{GM}} = 100$
 280 $\text{m}^2 \text{s}^{-1}$, which yields a value $v_{\text{eddy}} = 0.5 \text{ m}^2 \text{s}^{-1}$ similar to the value $v_{\text{eddy}} = \sigma \kappa_{\text{bot}} = 0.4 \text{ m}^2 \text{s}^{-1}$
 281 proposed by Callies (2018) and Holmes et al. (2019), where σ is the turbulent Prandtl number.
 282 We use a constant r since the parameterization is meant to be a crude placeholder for boundary
 283 layer restratification. To our relief, supplementary sensitivity experiments showed that watermass
 284 transformations and the boundary layer structure are relatively insensitive to the friction parameter
 285 r , in agreement with CF18. The linear drag parameter is small enough that the frictional terms
 286 are negligible in the interior where the flow is approximately geostrophic and are important only
 287 in near-boundary flows (both the deep western boundary currents and the abyssal mixing layers
 288 along the mid-ocean ridge) where the horizontal velocities are large (Salmon 1992, CF18). The
 289 choice of $r = 1.2 \times 10^{-5} \text{ s}^{-1}$ gives a non-dimensional value $\hat{r} = \frac{r}{\beta L} = 0.1$ such that the width of

290 the Stommel and Arons (1959b,a) deep western boundary currents is one-tenth the domain width
291 (see Section 3d).

292 *b. Geometry and boundary conditions*

293 We configure the PGCM to approximate the leading-order structure of a typical cross-
294 hemispheric abyssal ocean basin with a rectangular basin of zonal width $L = 3000$ km and merid-
295 ional length $2L = 6000$ km. Our idealized basin contains a mid-ocean ridge caused by seafloor
296 spreading in the middle and is bounded in the west, east, and north by continental slopes (Figure
297 2a). Although the southern region in our configuration ($y < -L/2 = -3000$ km) is also zonally
298 bounded, it should be thought of as a Southern Ocean-like sponge layer. In this southern region,
299 the transformation of deep waters into bottom waters arising from complex circumpolar channel
300 dynamics (e.g. as described in Marshall and Speer 2012) are parameterized by an idealized buoy-
301 ancy restoring forcing which pins the buoyancy field to a reference vertical profile (described in
302 detail in the next Section 3c). The model extends from $z = -2500$ m at the upper boundary to a
303 maximum depth of $z = -5000$ m and should be interpreted as representing only the diabatic lower
304 cell of the meridional overturning circulation. The idealized configuration can be thought to apply
305 locally to the Atlantic, Pacific, and Indian Ocean basins below $z = -2500$ m, which in the present
306 climate are all bounded by topography in the west, east, and north and have roughly meridionally-
307 aligned mid-ocean ridges (e.g. those highlighted in Figure 12). The idealized continental slopes
308 are half-Gaussian and the mid-ocean ridge is Gaussian in the zonal direction and tapers down
309 to zero meridionally in the southern restoring region to allow unconstrained zonal flows to close
310 the circulation of interest in the diffusively-forced basin to the north. The characteristic seafloor
311 slopes of roughly $\tan(\theta_{ridge}) \simeq 2 \times 10^{-3}$ for the mid-ocean ridge and $\tan(\theta_{cont.}) \simeq 4 \times 10^{-3}$ for the
312 continental slope are inspired by the South Atlantic, where the abyssal mixing layers and large-

313 scale abyssal circulation are best constrained by existing observations (Hogg et al. 1982; Polzin
 314 et al. 1997; Ledwell et al. 2000; St. Laurent et al. 2001; Thurnherr et al. 2005). The PGCM is
 315 bounded from above by assuming isopycnals are flat, i.e. $b = 0$ at $z = -2500$ m, which is approxi-
 316 mately valid in all basins north of the Southern Ocean (Talley 2007; Koltermann et al. 2011; Talley
 317 2013b). The PGCM is bounded from below by an insulating seafloor, $\mathbf{n} \cdot \nabla b = 0$ at $z = -d(x, y)$,
 318 where $d(x, y)$ is the seafloor depth and \mathbf{n} is the unit vector normal to the boundary.

319 *c. Buoyancy forcing*

320 The abyssal circulation in our model is forced by two competing diabatic terms in the buoy-
 321 ancy equation: minus the divergence of the turbulent buoyancy flux $-\nabla \cdot (-\kappa \nabla b)$, which has a
 322 positive integral contribution (diapycnal upwelling); and restoring to a reference buoyancy pro-
 323 file $-\lambda(b - B)$, which must necessarily have a negative integral contribution (diapycnal down-
 324 welling). Available potential energy is produced by parameterized turbulent mixing and converted
 325 into kinetic energy via the buoyancy production term $u^z b$ to drive a planetary-geostrophic abyssal
 326 circulation and balance the available potential energy loss due to restoring.

327 *(i) Turbulent mixing*

328 The prescribed turbulent diffusivity $\kappa = \kappa(x, y, z)$ is everywhere bottom-enhanced with a contri-
 329 bution equal to $\kappa_{\text{bot}} \exp\{-(z + d)/h\}$ over the mid-ocean ridge, where we choose $\kappa_{\text{bot}} = 5 \times 10^{-3}$
 330 m^2s^{-1} and $h = 250$ m to roughly match observations in the Brazil Basin (Figure 11). The bottom-
 331 enhanced contribution to κ is reduced by a factor of 20 to $\frac{\kappa_{\text{bot}}}{20} \exp\{-(z + d)/h\}$ over the con-
 332 tinental slopes to reflect the observed weakness of local wave-driven turbulence over smooth
 333 continental slopes (Figure 11 and Polzin et al. 1997). A uniform weak background diffusivity
 334 $\kappa_{\text{bg}} = \frac{\kappa_{\text{bot}}}{200} = 2.5 \times 10^{-5} \text{m}^2\text{s}^{-1}$ is added to stabilize the numerical solution, yielding a total diffu-

335 sivity distribution

$$\kappa(x, y, z) = \kappa_{bg} + \begin{cases} \kappa_{bot} \exp\{-(z + d(x, y))/h\}, & \text{if } L/2 < x < 3L/2 \text{ (mid-ocean ridge)} \\ \frac{\kappa_{bot}}{20} \exp\{-(z + d(x, y))/h\}, & \text{else (continental slopes),} \end{cases} \quad (10)$$

336 with a smoothing function applied over a horizontal distance of $L/10$ near the transitions at $x = L/2$
 337 and $x = 3L/2$. The net effect of this prescribed mixing is to power a diabatic upwelling along the
 338 mid-ocean ridge, where mixing is vigorous.

339 *(ii) Buoyancy restoring in the southern restoring region*

340 The prescribed restoring rate λ is has a meridional dependence

$$\lambda(y) = \lambda_0 \left[0.5 \left(1 - \tanh \left(\frac{y + L/2}{10L} \right) \right) \right], \quad (11)$$

341 which is equal to $\lambda_0 \simeq (10 \text{ years})^{-1}$ in the southern restoring region and vanishes rapidly north-
 342 wards, $\lambda \rightarrow 0$ as $y > -L/2$. The prescribed restoring rate is chosen based on the baroclinic ad-
 343 justment timescale given by a lateral diffusive timescale $\tau_{SO} = L_{SO}^2 / \kappa_{GM} = \frac{(10^6 \text{ m})^2}{3000 \text{ m}^2 \text{ s}^{-1}} \simeq 10 \text{ years}$,
 344 determined for an isopycnal diffusivity $\kappa_{GM} \simeq 3000 \text{ m}^2 \text{ s}^{-1}$ (Abernathey et al. 2013) and a South-
 345 ern Ocean of width $L_{SO} \simeq 1000 \text{ km}$. This restoring rate is much faster than the vertical diffusive
 346 timescale which spins up the overturning circulation $\tau_{mix} = H^2 / \bar{\kappa} \simeq 1000 \text{ years}$, where $H = 2500$
 347 m is the maximum thickness of the abyssal ocean and $\bar{\kappa} \simeq 10^{-4} \text{ m}^2 \text{ s}^{-1}$ is the volume-weighted
 348 mean diffusivity in the basin. Thus, the stratification in the southern restoring region does not
 349 deviate much from the prescribed profile (see Figure 7). The net effect of this parameterized
 350 buoyancy forcing in the southern restoring region is to transform deep waters into bottom waters
 351 (diabatic downwelling) to balance the transformation of bottom waters into deep waters (diabatic
 352 upwelling) driven by mixing along the mid-ocean ridge in the basin to the north. In contrast to
 353 CF18, we allow reference buoyancy profiles $B(z)$ corresponding to vertically-varying stratification

354 $\partial_z B = N^2(z)$, complicating the interpretation of the solution in terms of one-dimensional boundary
 355 layer dynamics which require a constant interior stratification N_0^2 .

356 *d. Dimensional parameters and scaling*

357 While the PGCM is discussed in dimensional terms, the PGCM is formulated and implemented
 358 non-dimensionally. The following dimensional scales,

$$\begin{aligned}
 L &= 6000 \text{ km} && \text{(basin width),} \\
 H &= 2500 \text{ m,} && \text{(abyssal ocean vertical extent),} \\
 \beta &= 2 \times 10^{-11} \text{ m}^{-1} \text{ s}^{-1}, && \text{(meridional gradient of Coriolis parameter),} \\
 N^2 &= 1.5 \times 10^{-6} \text{ s}^{-2}, && \text{(reference stratification at } z = -2500 \text{ m),} \\
 \kappa_{bot} &= 5 \times 10^{-3} \text{ m}^2 \text{ s}^{-1}, && \text{(diffusivity at the mid-ocean ridge seafloor),} \\
 r &= 1.2 \times 10^{-5} \text{ s}^{-1}, && \text{(frictional parameter),}
 \end{aligned}$$

359 are used to non-dimensionalize the system, with the coordinate transformation

$$x = L\hat{x}, \quad y = L\hat{y}, \quad z = H\hat{z} \quad (12)$$

360 and the substitutions

$$t = \frac{\beta L^3}{N^2 H^2} \hat{t}, \quad b = N^2 H \hat{b}, \quad p = N^2 H^2 \hat{p}, \quad (13)$$

$$u^x = \frac{N^2 H^2}{\beta L^2} \hat{u}^{\hat{x}}, \quad u^y = \frac{N^2 H^2}{\beta L^2} \hat{u}^{\hat{y}}, \quad u^z = \frac{N^2 H^3}{\beta L^3} \hat{u}^{\hat{z}}. \quad (14)$$

361 For reference, the non-dimensional time $\hat{t} = 1$ corresponds to $t = \tau \simeq 10$ years, where $\tau \equiv$

362 $\beta L^3 / N^2 H^2$. While the basin scale circulation takes a long time $\tau_{\text{mix}} = H^2 / \bar{\kappa} \simeq 1000$ years $\gg \tau$ to

363 spin up, the abyssal mixing layers are spun up on a fast timescale $\tau_{\text{BL}} = q^{-2} / \kappa_{\text{bot}} \simeq 1$ year $\ll \tau$,

364 where

$$q^{-1} = \sqrt{\frac{\kappa_{\text{bot}}(f^2 + r^2)}{rN^2 \tan^2 \theta}} \simeq 400 \text{ m} \quad (15)$$

365 is the thickness of the mixing layer predicted by 1D theory (CF18), $\kappa_{\text{bot}} = 5 \times 10^{-3} \text{ m}^2/\text{s}$ is the

366 diffusivity at the seafloor, and $f = \beta L/2$ is a representative value of the Coriolis parameter.

367 The non-dimensionalized equations (see CF18) depend only on the non-dimensional parameters

$$\hat{\alpha} = \frac{H}{L}, \quad \hat{\kappa} = \frac{\kappa\beta L^3}{N^2 H^4}, \quad \hat{r} = \frac{r}{\beta L}, \quad (16)$$

368 where $\hat{\alpha}$ is the aspect ratio of the basin; $\hat{\kappa} = \tau/\tau_{\text{mix}}$ is the ratio of the cross-basin propagation
369 timescale of long Rossby waves (with $f = \beta L$)

$$\tau \equiv L/c_g = L/\frac{\beta L^{-2}}{(NH/f)^2} = \frac{\beta L^3}{N^2 H^2}, \quad (17)$$

370 to the diffusive spin-up timescale $\tau_{\text{mix}} \equiv H^2/\bar{\kappa}$. \hat{r} is the ratio of the Stommel (1948) western
371 boundary layer width r/β to the basin width L . Since the prescribed κ is spatially-dependent,
372 the non-dimensional diffusivity $\hat{\kappa}$ inherits its spatial dependence in the numerical implementa-
373 tion. Scaling κ by using the volume-weighted average value $\bar{\kappa}$ in τ_{mix} gives $\hat{\kappa} = \tau/\tau_{\text{mix}} \simeq 0.01$.
374 Because the imposed turbulent diffusivity is isotropic, the small aspect ratio $\hat{\alpha} \sim 5 \times 10^{-4}$ re-
375 sults in a non-dimensionalized horizontal diffusivity many orders of magnitude smaller than the
376 non-dimensionalized vertical diffusivity, which is difficult to implement numerically. Instead,
377 we artificially increase the horizontal diffusivity for numerical stability by increasing the as-
378 pect ratio parameter to $\hat{\alpha} = 0.2$. This parameter only enters in the horizontal diffusion term
379 $\hat{\alpha}^2 [\partial_{\hat{x}} (\hat{\kappa} \partial_{\hat{x}} \hat{b}) + \partial_{\hat{y}} (\hat{\kappa} \partial_{\hat{y}} \hat{b})]$ (CF18) and remains small enough that it does not qualitatively af-
380 fect the results presented here, as evidenced by the negligible role of horizontal buoyancy fluxes
381 in the watermass transformations (Figure 5).

382 *e. Numerical implementation*

383 The model is formulated in terrain-following coordinates to accurately resolve the thin mixing-
384 driving flows along the sloped bottom boundary. The numerical implementation is described in
385 CF18. The Julia (Bezanson et al. 2017) implementation is available at <https://github.com/>

386 joernc/pgcm. The input files, output files, and post-processing notebooks necessary to replicate
387 the study are available at <https://github.com/hdrake/AbysalFlow> (Drake 2020).

388 **4. Abyssal Circulation Controlled By Mixing Layer Dynamics**

389 We begin by describing the general structure of the abyssal circulation at equilibrium in the
390 PGCM, i.e. at $\hat{t} = 50$ or $t \simeq 500$ years $\simeq \tau_{\text{mix}}$, when buoyancy tendencies have become sufficiently
391 small (Figure 7a). The stratification in the PGCM solution presented in this section is restored to
392 an exponential profile with a decay scale of $\delta = 1000$ m in the southern region (solid red dashed
393 line in Figure 2), which exhibits vertical variations of similar magnitude to those observed in the
394 Southern Ocean (black solid line). This is arguably our most “realistic” simulation of the abyssal
395 ocean and hereafter we refer to it as PGCM-REAL.

396 *a. Abyssal Mixing Layers and Deep Western Boundary Currents*

397 Figure 3 (a-c) shows the three Cartesian components of the abyssal flow field along a zonal sec-
398 tion 3000 km north of the equator. In the abyssal mixing layers spanning both flanks of the mid-
399 ocean ridge, buoyancy surfaces plunge to intersect the seafloor at a right angle (visually distorted
400 by the aspect ratio) to satisfy the no-flux boundary condition. As expected from 1D theory (CF18),
401 the boundary flows are thicker and stronger over the mid-ocean ridge where mixing is strong than
402 over the continental slopes where mixing is weak. In the bottom boundary layer (BBL), plung-
403 ing buoyancy surfaces drive frictionally-balanced upwelling (Figure 3c) and frictional-geostrophic
404 flow opposite the direction of Kelvin wave propagation (Figure 3b), i.e. anti-cyclonic in the north-
405 ern hemisphere. In the stratified mixing layer (SML) just above the BBL, buoyancy surfaces are
406 at leading order flat and the bottom-enhanced mixing drives downwelling (Figure 3c), as expected
407 from the vertical advection-diffusion balance (eq. 3) reviewed in Section 2.

408 Net diapycnal upwelling in the Northern Hemisphere can be inferred from the meridional flow
 409 field at the equator: dense bottom waters flow into the northern hemisphere and relatively lighter
 410 deep waters flow out (Figure 3e). Since the Coriolis force vanishes at the equator, the buoyant force
 411 associated with the bending of buoyancy surfaces to satisfy the bottom-boundary condition can
 412 only be balanced by a cross-slope frictional flow (Figure 3d,f) and any along-slope flows associated
 413 with the abyssal mixing layers vanishes (compare Figure 3e to Figure 3b). The only meridional
 414 flow are Stommel (1948)-like deep western boundary currents (DWBC) along the continental slope
 415 on the western side of the domain and the eastern flank of the ridge (Figure 3e). In this particular
 416 configuration, a southward-flowing DWBC develops on the eastern flank of the ridge near its crest
 417 and is much weaker than the DWBC on the western continental slope. The southward DWBC on
 418 the ridge is relatively intensified in simulations with a taller ridge.

419 *b. Depth-integrated and Overturning Circulations*

420 The global abyssal circulation is more intuitively visualized by considering the three Cartesian
 421 streamfunctions that describe the flow, which we compute by integrating the u^x , u^y , and u^z veloc-
 422 ities in x , y , and z , respectively³ (Figure 4). Figure 4b shows the familiar streamfunction for the
 423 meridional overturning circulation (MOC) in the y - z plane, which should be thought of as corre-
 424 sponding to the lower-cell of the global MOC. This circulation has a strength of about 1.6 Sv at
 425 the equator, with water 1) downwelling diabatically in the southern restoring region, 2) flowing
 426 northwards to fill the abyssal depths, 3) gradually upwelling along the length of the basin, and 4)
 427 returning to the southern restoring region to close the circulation. We note in particular that the

³Integrating the continuity equation in $\frac{\partial u^x}{\partial x} + \frac{\partial u^y}{\partial y} + \frac{\partial u^z}{\partial z} = 0$ along any of the three directions x , y , or z and imposing the no-normal flow boundary condition yields an equation of the form $\int \left(\frac{\partial u^{x_1}}{\partial x_1} + \frac{\partial u^{x_2}}{\partial x_2} + \frac{\partial u^{x_3}}{\partial x_3} \right) dx_3 = \frac{\partial U^{x_1}}{\partial x_1} + \frac{\partial U^{x_2}}{\partial x_2} = 0$, where x_1, x_2, x_3 are permutations of x, y, z , $U^{x_1} = \int u^{x_1} dx_3$ and $U^{x_2} = \int u^{x_2} dx_3$. The resulting non-divergent flow field can then be expressed as a streamfunction ψ_3 defined by $\mathbf{U} = U^{x_1} \mathbf{x}_1 + U^{x_2} \mathbf{x}_2 = (-\nabla \times \psi_3 \mathbf{x}_3)$.

428 MOC extends all the way from the ocean seafloor to the top of the mid-ocean ridge, in contrast
429 to the MOC in the CF18 framework, in which significant overturning is confined to the base of
430 topographic slopes (see Section 6c for a discussion on the role of the ridge height in setting the
431 vertical extent of the MOC).

432 The up- and down-welling in the abyssal mixing layers is evident in the zonal overturning
433 streamfunction in the x - z plane, which shows upwelling in a thin BBL and broader downwelling
434 in the SML above (Figure 4c). The upwelling in bottom boundary layers is confined to the two
435 flanks of the mid-ocean ridge, where mixing is vigorous and bottom-enhanced, and is negligible
436 over the weakly-mixed continental slopes. In this case, the upwelling and downwelling transports
437 are equal and opposite in strength, i.e. the circulation closes, because the downwelling flow in-
438 cludes both the residual diabatic upwelling along the ridge as well as the net diabatic downwelling
439 by the restoring condition in the southern region, which is concentrated on the eastern continental
440 slope. Nonetheless, the zonal overturning streamfunction provides a qualitative sense of the zonal
441 overturning circulations driven by mixing layer dynamics along the mid-ocean ridge.

442 The depth-integrated circulation in our simulations stands in contrast to that of Stommel and
443 Arons (1959a)'s barotropic model and is the expression of a combination of various baroclinic
444 deep western boundary currents and mixing layer flows (Figure 4a). Within 2000 km of the equa-
445 tor, the northward and southward components of the deep western boundary currents alternatively
446 dominate (compare with the meridional velocity at the equator in Figure 3). North of $y = 2000$ km,
447 the depth-integrated circulation is dominated by the along-slope flow in the bottom boundary layer,
448 which is opposite the direction of Kelvin wave propagation. The depth-integrated circulation is
449 strongly influenced by mixing layer dynamics, both near the boundaries and in the interior, and
450 is structurally distinct from that predicted by the linear response to vortex stretching alone (Stom-
451 mel and Arons 1959b; Pedlosky 1992; Cember 1998). Sverdrup balance only holds far from the

452 boundaries and accounts for little of the net transport compared to the abyssal mixing layer and
453 western boundary current flows, where friction is important.

454 *c. Partially-Compensating Watermass Transformations*

455 The watermass transformation represents the net flow across a buoyancy surface driven by di-
456 abatic forcing. Watermass transformation in the PGCM is driven by: 1) bottom-enhanced turbu-
457 lent mixing (positive in the net) and 2) restoring to a reference buoyancy profile in the southern
458 restoring region (negative in the net). In the northern hemisphere, the restoring rate vanishes by
459 construction and watermass transformation is dominated by the mixing-driven component. Its
460 calculation, following Walin (1982) and Ferrari et al. (2016), is given by

$$T(b) = \frac{\partial}{\partial b} \int_{V_{b' < b}} \nabla \cdot (\kappa \nabla b') dV, \quad (18)$$

461 where $V_{b' < b}$ is the volume of water less buoyant than b . Watermass transformation is conveniently
462 expressed in units of volumetric transport (m^3/s) and can be decomposed into various contribu-
463 tions. When applied to regions of bottom-enhanced mixing in the abyss, it is informative to de-
464 compose the net watermass transformation into the typically negative contribution (balanced by
465 diapycnal downwelling) in the SML and the typically positive contribution (balanced by diapycnal
466 upwelling) in the BBL (e.g. Ferrari et al. 2016; McDougall and Ferrari 2017). For the purposes
467 of watermass transformation calculations in this paper, we define the BBL as the layer with a
468 convergent buoyancy flux, $\nabla \cdot (\kappa \nabla b) > 0$, which extends upwards from the seafloor to the level
469 at which buoyancy flux attains its maximum magnitude; the remainder of the ocean is considered
470 the SML and is dominated by a buoyancy flux divergence, $\nabla \cdot (\kappa \nabla b) < 0$. For convenience, all
471 watermass transformations in this paper are computed in buoyancy space and remapped into depth

472 space according to the average depth of buoyancy surfaces,

$$\bar{z}(b) = \frac{1}{A(b)} \int z(b) dA, \quad (19)$$

473 which facilitates comparison across simulations with dramatically different stratifications and
 474 against the fixed depths of topographic features in the ocean.

475 The net northern hemisphere watermass transformation of $T_{\text{net}} = 1.6$ Sv at 3750 m (Figure 5a),
 476 where it reaches its maximum, is consistent with the depth and magnitude of the maximum of
 477 the MOC streamfunction at the equator (Figure 4b). The net watermass transformation $T_{\text{net}} =$
 478 $T_{\text{BBL}} + T_{\text{SML}} = 1.6$ Sv (black line) is the residual of a positive contribution of $T_{\text{BBL}} = 2.1$ Sv from
 479 the BBL (red line) and a negative contribution of $T_{\text{SML}} = -0.5$ Sv from the SML (blue line), both
 480 of which are dominated by the vertical component of the buoyancy flux divergence (dashed lines),
 481 i.e.

$$T(b) = \partial_b \int_{V_{b' < b}} \nabla \cdot (\kappa \nabla b') dV \simeq \partial_b \int_{V_{b' < b}} \partial_z (\kappa \partial_z b') dV. \quad (20)$$

482 Virtually all of this transformation occurs on the flanks of the mid-ocean ridge (compare Figure
 483 5a,b).

484 For the convenience of being able to ignore meridional variations in the basin geometry (and
 485 their effects on watermass transformations via the “perimeter” effect, as described by Holmes
 486 et al. 2018), we limit the remaining discussion to a domain from $L/2 < x < 3L/2$ and $0 < y < L/2$
 487 along the north-hemisphere mid-ocean ridge, which is responsible for roughly 1 Sv of the full
 488 basin’s transformation (Figure 5c; limited domain outlined in Figure 2a).

489 The net watermass transformation $T_{\text{net}} = 1$ Sv at equilibrium is much larger than the $L\Psi_{\text{bg}} \leq$
 490 0.1 Sv predicted by the integral constraint (eq. 5) from 1D boundary layer theory. To clarify
 491 the discrepancy between the watermass transformations that emerge from the 3D PGCM and the

492 watermass transformations predicted by 1D dynamics, we emulate the 3D PGCM simulation by
 493 solving the 1D boundary layer equations locally and interpolating onto the 3D PGCM grid.

494 **5. Emulating the 3D PGCM with local 1D boundary layer models**

495 *a. Boundary layer theory*

496 Following CF18, we transform the planetary-geostrophic equations (6) - (8) from the Cartesian
 497 coordinates (x, y, z) to a coordinate system (x', y', z') aligned with an infinitely extending sea floor at
 498 $z = x \tan \theta$, with slope angle θ , and ignoring the southern region restoring condition on buoyancy.
 499 The transformation is given by $x' = x \cos \theta + z \sin \theta$, $y' = y$, $z' = -x \sin \theta + z \cos \theta$. Buoyancy
 500 $b = B(z) + b'$ is decomposed into a background $B(z)$ with constant stratification $\partial_z B = N_0^2$ and an
 501 anomaly $b'(z')$. The steady state boundary layer equations are thus given by:

$$-f \cos \theta u^{y'} = b' \sin \theta - r \cos \theta^2 u^{x'} \quad (21)$$

$$f \cos \theta u^{x'} = -r u^{y'} \quad (22)$$

$$u^{x'} N_0^2 \sin \theta = \partial_{z'} [\kappa (N^2 \cos \theta + \partial_{z'} b')], \quad (23)$$

502 with a no-flux boundary condition $\partial_{z'} b' + N_0^2 \cos \theta = 0$ at the seafloor $z' = 0$ and decay conditions
 503 $\partial_{z'} u^{x'}, \partial_{z'} u^{y'}, \partial_{z'} b' \rightarrow 0$ as $z' \rightarrow 0$. These equations yield exact analytical solutions for constant κ
 504 (CF18) and approximate analytical solutions for elementary $\kappa(z)$ profiles (Callies 2018).

505 *b. Emulator setup*

506 We emulate the PGCM solution by using finite differences to solve the time-dependent
 507 boundary-layer equations (21) - (23) with the local Coriolis parameter $f(y)$ and slope angle $\theta(x, y)$
 508 at each $(x, y) = (\xi, \eta)$ of the PGCM grid, which is a sensible approach given that the parameters
 509 $f(y)$ and $\theta(x, y)$ vary on scales larger than the those of the boundary-layer solutions (Dell and Pratt

510 2015). Since these local boundary layer solutions are given in terms of the local slope-normal di-
511 rection z' rather than the true vertical direction z , we project the solution onto the true vertical
512 direction z with the substitution $z' \rightarrow z/\cos\theta$ and linearly interpolate from the projected z -levels
513 of the boundary layer solution to the PGCM's local σ -levels. This process provides an emulator
514 of the PGCM which is purely the result of local 1D dynamics but is re-gridded to the same grid as
515 the 3D PGCM and can thus be directly compared.

516 *c. Emulator evaluation*

517 We evaluate the emulator against the spin-up of a PGCM simulation with a constant stratification
518 initial condition N_0^2 , hereafter PGCM-CONST. The 1D emulator accurately reproduces the initial
519 spin-up of buoyancy and velocity fields of the PGCM-CONST simulation along most of the mid-
520 ocean ridge flanks, but fails at the top and bottom of the ridge where the topographic curvature is
521 large and the cross-slope convergences omitted by 1D dynamics become important (Figure 6a,b).

522 As the solution nears equilibrium, however, the interior basin stratification drifts away from its
523 constant initial value (compare gray and black contours in Figure 6d) and the boundary layer flows
524 diverge from the 1D emulator's prediction (Figure 6c,d). This is expected, as the basin stratification
525 of PGCM-CONST is allowed to evolve in response to the 3D circulation while the background
526 interior stratification N_0^2 is a constant parameter in the emulator. Relative to the emulator, the
527 equilibrium PGCM-CONST solution exhibits reduced downwelling in the SML and enhanced
528 upwelling in the BBL, both of which contribute to enhancing the net diapycnal upwelling. In
529 Section 6, we use the 1D emulator to identify properties of the watermass transformations in the
530 PGCM that can be explained by one-dimensional dynamics alone.

531 **6. The Effect of Variable Interior Stratification on the Abyssal Circulation**

532 *a. What sets the abyssal stratification?*

533 In our PGCM simulations, the drift of interior buoyancy surfaces over time (Figure 6d) suggests
534 that the interior stratification at equilibrium may differ substantially from the stratification of the
535 southern region buoyancy profile. Figure 7a shows the temporal evolution of the horizontally-
536 averaged vertical stratification profile, averaged over the northern hemisphere basin in the PGCM,
537 where darker greys represent later times. In PGCM-CONST, the abyssal stratification develops
538 substantial vertical structure in the basin over time, despite being rapidly restored back to a con-
539 stant stratification in the southern restoring region (solid lines, Figure 7a). Net watermass trans-
540 formation is initially unbalanced by Eulerian diapycnal flow (compare Figure 8b,f) and thus drives
541 changes in the volume of buoyancy layers, which can be interpreted as a component of the diapy-
542 cnal transport due to the velocity of buoyancy surfaces (Marshall et al. 1999). Excess watermass
543 transformations near the base of the slope destroy the densest layers and expand the deep layers,
544 which translate into a reduction of the stratification that originates at the bottom of the ridge and
545 propagates upwards over time. The details of the vertical structure of the equilibrium basin strati-
546 fication depend on ridge height (not shown), but in all cases the basin stratification increases from
547 zero at the maximum depth (imposed by the no-flux condition at the flat bottom) up to near the
548 restoring reference value of N_0^2 at the top boundary.

549 The zonal-mean basin stratification develops a significant meridional structure, wherein the
550 zonal-mean stratification along the ridge weakens with distance from the Southern restoring re-
551 gion (Figure 7b,c). In contrast to the mixing layer stratification, which is strongest at the equa-
552 tor and weaker polewards (Callies 2018, CF18), the zonal-mean stratification decreases roughly
553 monotonically with increasing latitude.

554 Simulations using a reference buoyancy profile that corresponds to an exponential stratification
555 with decay scale of $\delta = 1000$ m exhibit much less drift in their stratifications over time (dashed
556 lines, Figure 7a,b). Although the equilibrium basin stratifications in all of the different PGCM
557 experiments develop vertical structure, there does not seem to be a single preferred equilibrium
558 stratification that depends only on the mixing: both the geometry of the abyssal topography and the
559 restoring profile in the southern restoring region influence the interior stratification at equilibrium.

560 *b. Effect of variable stratification on watermass transformations*

561 We begin by considering the case of transient spin-up from a reference buoyancy profile with
562 constant stratification N_0^2 , PGCM-CONST. It is useful to consider the evolution of the PGCM
563 during its initial spin-up ($\hat{t} \simeq \tau_{\text{BL}}/\tau = 0.1$) when only mixing layer dynamics are relevant and
564 the solution is thus well-predicted by the 1D Emulator (Figure 6). Figure 8a shows the water-
565 mass transformations in the 1D Emulator at $\hat{t} = 0.1$, which almost exactly predicts the watermass
566 transformations in the full 3D PGCM (Figure 8b).

567 Between $-4200 \text{ m} < z < -3000 \text{ m}$, where the slope of the mid-ocean ridge is roughly constant,
568 the near-boundary flow exhibits a vanishingly small net transport (solid black line in Figure 8a),
569 which is approximately equal to the integral constraint $T_{\text{net}} \simeq L\Psi_{\text{bg}} = L\kappa_{\text{bg}} \cot \theta \leq 0.1$ Sv predicted
570 by 1D boundary layer theory (dashed black line in Figure 8a). This vanishingly small net transport
571 is the result of large positive transformation T_{BBL} (diabatic upwelling, in red) in the BBL and
572 almost-as-large negative transformation T_{SML} (diabatic downwelling, in blue) in the SML. Below
573 $z = -4200$ m, at the base of the topographic slope, abyssal bottom waters feed the upwelling in the
574 BBL and the maximum net watermass transformation is well predicted by the strictly upwelling
575 transport in the bottom boundary layer from 1D theory (Figure 8a,b), as suggested by CF18.

576 For the spin-up from a reference stratification that increases exponentially with height (as is al-
 577 most ubiquitously the case in the abyssal ocean), the integral constraint (eq. 5) no longer holds at
 578 $\hat{t} = 0.1$ and the solution already exhibits a net transformation much larger than $L\Psi_{bg}$ at all depths
 579 from the base of the slope to the ridge crest (Figure 8c,d). The increase in the net transformation,
 580 which spans the full vertical extent of the ridge, is primarily due to a decrease in the downwelling
 581 in the SML which, in the extreme case of an exponential scale height of $\delta = 500$ m for the restor-
 582 ing stratification, vanishes completely (Figure 8d). The strongly positive net transformation is
 583 primarily due to the buoyancy convergence driven by the rapid increase of the initial stratification
 584 with height, i.e. $\kappa\partial_{zz}B > 0$ reduces the divergence $\nabla \cdot (\kappa\nabla b) < 0$ due to $\partial_z\kappa < 0$ in the SML (see
 585 also Figure 14).

586 As these solutions reach equilibrium, they retain a finite net transformation at all depths from
 587 the base of the slope to the ridge crest, slightly reduced by gradually strengthening negative trans-
 588 formations in the SML (compare Figure 8g,h to Figure 8c,d). At equilibrium, we find the degree
 589 of compensation near the ridge crest depends on the vertical scale over which the restoring stratifi-
 590 cation varies (within a range applicable to the ocean): the more rapidly the stratification increases
 591 with height, the less upwelling in the BBL is compensated by downwelling in the SML (Figure 8f-
 592 h and Figure 9a). In contrast, upwelling in the BBL is remarkably invariant to vertical variations in
 593 the stratification and remains a reasonable prediction for the maximum net transformation (Figure
 594 9a,b), which occurs at the base of the slope where the compensating downwelling contribution
 595 from the SML vanishes (Figure 9c). Thus, while the maximum net watermass transformation is
 596 accurately predicted by upwelling in the BBL alone, the vertical structure and extent of watermass
 597 transformations depend also on downwelling in the SML, which itself is strongly dependent on
 598 the vertical stratification, and is not predicted by 1D theory.

599 *c. Vertical extent of overturning set by ridge height*

600 We have shown that most of the watermass transformation occurs within abyssal mixing layers
601 along the mid-ocean ridge (Figure 5a,b). We further hypothesize that variations in the height of
602 the ridge modulate the vertical extent of abyssal watermass transformations and thus the vertical
603 extent of the abyssal overturning cell. We test this hypothesis by running variations of the PGCM-
604 CONST where we vary the ridge height from 500 m to 2000 m, in increments of 500 m. In the
605 initial spin-up, largely compensating positive and negative transformations develop in the BBL
606 and SML, respectively, from the base of the ridge slope up to the ridge crest (Figure 10a-d). The
607 net transformation below the ridge crest vanishes according to the integral constraint (eq. 5),
608 except near the sea-floor where bottom water feeds into the BBL. At equilibrium, however, the
609 stratification drifts away from its constant reference state (e.g. Figure 7) and permits a finite net
610 transformation (Figure 10e-h), which spans the full vertical extent of the ridge. The result that the
611 vertical extent of the abyssal MOC follows the vertical extent of the mid-ocean ridge is consistent
612 with Lumpkin and Speer (2007)'s global inversion for the MOC, which shows that the vertical
613 extent of the Atlantic and Indo-Pacific lower MOC cells appear to closely follow the vertical
614 extent of their respective major bathymetric features (i.e. mid-ocean ridges).

615 **7. Comparison with realistic mid-ocean ridges**

616 The topography and mixing in the PGCM is inspired by observations from the Brazil Basin (Fig-
617 ure 11), one of the regions of the abyssal ocean best characterized by observations (e.g. St. Laurent
618 et al. 2001; Thurnherr and Speer 2003). The circulation that emerges from the PGCM-REAL sim-
619 ulation (Figure 11b) is qualitatively similar to the circulation inferred from observations using an
620 inverse model (Figure 11a, based on St. Laurent et al. 2001): bottom-enhanced mixing along the

621 slope of the mid-ocean ridge drives upwelling in a bottom boundary layer and downwelling in a
622 stratified mixing layer above.

623 To contextualize our simulated watermass transformations, we estimate watermass transforma-
624 tions in the ocean based on hydrography and a commonly-used mixing parameterization, follow-
625 ing Ferrari et al. (2016)’s modifications of Nikurashin and Ferrari (2013). The buoyancy flux is
626 parameterized by $\overline{w'b'} = -\Gamma\varepsilon$, where ε is the kinetic energy dissipation and Γ is a ‘mixing effi-
627 ciency’ set to $\Gamma = 0.2$ (Osborn 1980); the buoyancy field (computed from the neutral density γ) is
628 taken from a gridded product derived from hydrographic sections of the World Ocean Circulation
629 Experiment (Gouretski and Koltermann 2004); and we impose the insulating bottom boundary
630 condition $\mathbf{n} \cdot \overline{\mathbf{u}'b'} \simeq \overline{w'b'} = 0$ (where $\mathbf{n} \simeq \mathbf{z}$ for typical bathymetric slopes of $\tan \theta \ll 1$). The dis-
631 sipation rate ε is produced by applying linear wave radiation theory for internal tides (Nycander
632 2005) and lee waves (Nikurashin and Ferrari 2011) and assuming a fraction $q = 0.3$ of the radiated
633 energy is locally dissipated according to a bottom-enhanced structure function with a height scale
634 of 500 m (St. Laurent and Garrett 2002). We compare watermass transformation estimates from
635 the ocean with estimates from PGCM-REAL, a simulation with restoring to an exponential refer-
636 ence stratification with a decay scale of 1000 m and which is our simulation with a stratification
637 in the southern restoring region most similar to the Southern Ocean’s (Figure 2c). We focus on
638 rectangular regions with dimensions 3000 km by 3000 km (in the PGCM) or 30° longitude by 30°
639 latitude (in the ocean), which encompass comparable ridge lengths and surface areas at subtropical
640 latitudes. Watermass transformations in the PGCM-REAL simulation (Figure 12a) are the result
641 of partially compensating buoyancy flux convergence (Figure 12e) in the BBL (red colors) and
642 buoyancy flux divergence in the SML (blue colors). Qualitatively similar (but noisier) watermass
643 transformations emerge for the mid-ocean ridge regions in the Pacific, Atlantic, and Indian (Figure
644 12b-d, regions delineated by boxes in panels e,f). While the net transformation varies from 0.5

645 Sv in the South Pacific region to 2 Sv in the Indian Ocean region, the net transformation is al-
646 ways the result of partially compensating upwelling and downwelling. This qualitative similarity
647 emerges in the large-scale watermass diagnostic, despite the relatively heterogeneous nature of the
648 estimated buoyancy flux and topography in the ocean basins (compare Figure 12f, e), because in
649 all cases the turbulent buoyancy flux is bottom-enhanced (driving downwelling) and tapers to zero
650 over the last grid cell to meet the insulating boundary condition within some bottom boundary
651 layer (driving upwelling). This property of compensating watermass transformations is in contrast
652 to the case of a constant buoyancy flux (Ferrari et al. 2016; Holmes et al. 2018), in which there is
653 no compensating downwelling. Estimates of *global* abyssal watermass transformations, however,
654 exhibit stronger compensation by downwelling in the SML than shown here for mid-ocean ridge
655 regions (by factors of 2 and 3 for Ferrari et al. 2016 and McDougall and Ferrari 2017, respectively).
656 In Section 8 we present evidence in support of McDougall and Ferrari (2017)'s speculation that
657 much of this discrepancy arises due to the effects of correlations between the buoyancy flux and
658 the stratification, which are omitted in their calculations. Ferrari et al. (2016)'s estimate includes
659 these correlation terms but relies on poorly-sampled knowledge of the buoyancy flux and stratifi-
660 cation close to the seafloor, which likely introduces substantial uncertainty in their estimate. While
661 much work has gone into understanding how the compensation factor depends on various param-
662 eters of the diagnostic approach based on climatological observations and parameterized mixing
663 (McDougall and Ferrari 2017; Holmes et al. 2018; Cimoli et al. 2019), the functional dependence
664 of the compensation factor in the prognostic dynamic approach has received comparably little
665 attention and is not well known.

666 8. Classic recipes and new trends in abyssal cuisine

667 Quantitative study of the abyssal stratification began with the classic study of Munk (1966): a
 668 point-wise theory in which the observed abyssal stratification is the result of a balance between
 669 uniform upwelling and a uniform turbulent vertical mixing. As anticipated by Munk (1966), sub-
 670 sequent observations show turbulent mixing to be strongly heterogeneous, with an emerging pat-
 671 tern of weak background mixing and vigorous mixing near rough topography (Polzin et al. 1997;
 672 Waterhouse et al. 2014). In light of these observations, Munk and Wunsch (1998) revisited Munk
 673 (1966)’s theorized point-wise vertical balance and re-derive it as a horizontally-averaged buoyancy
 674 budget, which we transcribe as

$$\langle w \rangle A \simeq \langle N^2 \rangle^{-1} \frac{d}{dz} [A(z) \langle \kappa \rangle \langle N^2 \rangle] \quad (24)$$

675 in our notation, where the key assumption is that correlations between the turbulent diffusivity κ ,
 676 the stratification N^2 , and the vertical velocity w are all assumed to be negligible, such that $\langle w N^2 \rangle =$
 677 $\langle w \rangle \langle N^2 \rangle$ and $\langle \kappa N^2 \rangle = \langle \kappa \rangle \langle N^2 \rangle$. In Figure 13a,b,c, we show, respectively, the three terms in eq. 24:
 678 the horizontally-averaged stratification $\langle N^2 \rangle$, the turbulent buoyancy flux $\langle \kappa \rangle \langle N^2 \rangle$, and the isobath
 679 surface area (ocean area at a fixed depth) $A(z)$. In Figure 13d we show the left- and right-hand
 680 sides of eq. 24 in the PGCM-REAL simulation at equilibrium. The horizontally-averaged vertical
 681 flux divergence (right-hand side of eq. 24) is a poor prediction for the diagnosed vertical transport.
 682 This is not surprising, given that 1) w , N^2 , and κ are spatially-correlated in our solutions and 2) that
 683 density surfaces are strongly sloping near boundaries. Analysis in buoyancy coordinates, such as
 684 either the thickness-weighted average framework (De Szoeke and Bennett 1993; Young 2011) or
 685 the watermass transformation framework (Walín 1982), are more appropriate. The mixing-driven
 686 watermass transformation (solid black line) equals the diapycnal transport (the diabatic MOC of

687 interest here), by definition, but also serves as a better approximation of the vertical transport $\langle w \rangle A$
 688 than the right hand side of eq. 24.

689 In Figure 13c, we show that ignoring correlations within the buoyancy flux $\langle \kappa N^2 \rangle \approx \langle \kappa \rangle \langle N^2 \rangle$
 690 introduces large biases relative to the full horizontal-mean buoyancy flux, which results in even
 691 larger biases in the flux divergence (Figure 13d). To investigate the role of these spatial correlations
 692 between κ and N^2 more exactly, we return to the watermass transformation framework, where we
 693 now define $\langle \cdot \rangle \equiv A_b^{-1} \int_{A_b} \cdot dA$ as the average along a buoyancy surface. We can thus decompose the
 694 vertical component of the watermass transformation into uncorrelated and correlated components,
 695 respectively:

$$T_{\text{net}} \approx \partial_b (A \langle \kappa \partial_z b \rangle) = \partial_b (A \langle \kappa \rangle \langle \partial_z b \rangle) + \partial_b (A \langle \kappa' \partial_z b' \rangle), \quad (25)$$

696 where $\kappa' = \kappa - \langle \kappa \rangle$ and $\partial_z b' = \partial_z b - \langle \partial_z b \rangle$ are deviations from the mean along a buoyancy surface.
 697 Figures 14a,c show that ignoring the correlation terms in the watermass transformation results
 698 in an overestimation of the net transformation by 20% to 200% because the stratification $\partial_z b'$
 699 is locally reduced in the abyssal mixing layers where κ' is high (orange lines in Figure 14a,c),
 700 with the magnitude of this bias varying dramatically across simulations with different topographic
 701 geometries and restoring profiles.

702 To support our hypothesis that vertical variations in the stratification are necessary to support
 703 large net watermass transformations, we further decompose the uncorrelated component into a
 704 component related to the change in the mean stratification and a residual component related to
 705 changes in both the area of the buoyancy surface and the mean diffusivity, respectively:

$$\partial_b (A \langle \kappa \rangle \langle \partial_z b \rangle) = A \langle \kappa \rangle \partial_b \langle \partial_z b \rangle + (\partial_z b) \partial_b (A \langle \kappa \rangle). \quad (26)$$

706 In the experiment shown in Figure 14a,b, where the uncorrelated component is a reasonable ap-
 707 proximation of the net transformation, we find the net transformation to be largely driven by vari-

708 ations of the stratification with buoyancy, $A\langle\kappa\rangle\partial_b\langle\partial_z b\rangle$, although variations in the diffusivity in-
709 tegrated along a buoyancy surface are also important. Variations in the stratification also appear
710 important in the experiment shown in Figure 14d, although this decomposition is more difficult to
711 interpret since the uncorrelated component overestimates the net transformation by a factor of 3
712 (Figure 14c).

713 **9. Discussion**

714 The idealized numerical model presented here describes an abyssal circulation and stratification
715 controlled by mixing-driven flows along a mid-ocean ridge in a cross-equatorial basin (Figure
716 1). By initializing with- and restoring to- a series of reference buoyancy profiles in the south of
717 the basin, we investigate transient and equilibrium coupling between the basin stratification and
718 the mixing-driven boundary flows. At equilibrium, dense abyssal waters form in the southern
719 restoring region and flow north via adiabatic deep western boundary currents (red circle), filling
720 the abyssal depths in both hemispheres. Along the mid-ocean ridge, bottom-enhanced mixing
721 (squiggly lines) drives a net transformation of dense abyssal waters into lighter deep waters, the
722 residual of partially-compensating upwelling in a bottom boundary layer (BBL) and downwelling
723 in a stratified mixing layer (SML) right above it. The newly formed light deep waters flow zonally
724 towards the western continental slope (solid arrow), returning southward via an adiabatic deep
725 western boundary current to the restoring region (blue circles), and closing the abyssal overturning
726 circulation as they are once again transformed into dense abyssal waters.

727 Despite the extreme degree of idealization in our formulation of the Planetary Geostrophic Cir-
728 culation Model (PGCM), the watermass transformations that emerge at equilibrium are qualita-
729 tively similar to diagnostic estimates of watermass transformations near mid-ocean ridges in the
730 Pacific, Atlantic, and Indian Oceans (Figure 12), which are themselves fairly uncertain (Cimoli

731 et al. 2019). Similarly, the zonal overturning that emerges within bottom mixing-driven flows
732 along the mid-ocean ridge are qualitatively similar to that described by an inverse model of the
733 abyssal Brazil Basin based on in-situ measurements (St. Laurent et al. 2001, and Figure 11). Re-
734 maining differences between our simulations and observations are likely due to the crude nature
735 of our parameterizations for the restratification by submesoscale turbulence and for the formation
736 of bottom waters in the Southern Ocean, as well as uncertainties in the observational estimates.

737 The equilibrium interior stratification in the PGCM always exhibits dynamically significant ver-
738 tical variations, the structure of which is determined by a combination of mixing layer dynamics
739 and the restoring condition in the south. Even in our simulations that are initialized from- and
740 restored to- a constant stratification reference buoyancy profile, heterogeneities in the topographic
741 slope cause cross-slope divergence and a corresponding exchange flow between the abyssal mix-
742 ing layers and the interior. Over time, these exchange flows modify the interior stratification and
743 associated watermass transformations.

744 As in CF18, we find the prediction of upwelling in the BBL by one-dimensional (1D) boundary
745 layer theory provides a reasonable approximation to the maximum net transformation or, equiv-
746 alently, the strength of the diabatic meridional overturning circulation (Figures 8 and 9). While
747 this interpretation provides a useful prediction for the maximum net transformation which occurs
748 at the base of topographic slopes, it does not inform the net transformation along the flanks of the
749 mid-ocean ridge, where upwelling in the BBL is instead partially compensated by downwelling in
750 a SML. At depths where both the BBL and the SML are active, 1D theory predicts almost perfect
751 compensation and a resulting net transformation that is vanishingly small (eq. 5 and Figure 8a,e).
752 In contrast, our PGCM simulations exhibit finite net watermass transformations that extend from
753 the base of the ridge slopes all the way up to the ridge crest (Figure 10), consistent with both
754 our oceanic estimates (Figure 12) and inverse models of the Indo-Pacific overturning circulation

755 (Lumpkin and Speer 2007). We attribute the existence of a finite net transformation to vertical
756 variations in the basin stratification (Figures 8 and 14). As we increase the degree to which the
757 restoring stratification varies in the vertical, the compensation of BBL upwelling by SML down-
758 welling (evaluated near the depth of the ridge crest) ranges from nearly-perfect compensation to
759 nearly-zero compensation (Figure 9a). Thus, while 1D bottom boundary layer theory provides a
760 reasonable approximation to *maximum net* watermass transformation, the vertical extent and struc-
761 ture of watermass transformations depends on the degree of compensation by downwelling in the
762 SML, which is itself coupled to the vertically-varying basin stratification.

763 Our simulations show that correlations between mixing and stratification (Figure 14a,c), which
764 are typically ignored in idealized models of the zonal-mean abyssal overturning (Nikurashin and
765 Vallis 2011; Jansen and Nadeau 2019), can be of leading-order importance in abyssal watermass
766 transformations; whether these correlations are important in the ocean remains an open question.
767 Despite our improved understanding of the roles of bottom mixing and the interior basin strat-
768 ification on the abyssal watermass transformations and circulation, we fall short of a predictive
769 analytical theory for the abyssal overturning and stratification that couples boundary layer dynam-
770 ics with a model for the evolution of the interior stratification. Recent and ongoing work in 1)
771 observing abyssal mixing layers (e.g. Garabato et al. 2019), 2) investigating their dynamics with
772 idealized theory and simulations (Wenegrat et al. 2018; Callies 2018; Holmes et al. 2019), 3) de-
773 veloping and evaluating parameterizations of their turbulent fluxes, 4) and coupling them to the
774 basin stratification (e.g. refining the approach of Salmun et al. 1991) will all be key ingredients
775 for cooking up a revised theory of the abyssal circulation and stratification.

776 *Acknowledgments.* We thank Ali Mashayek, Laura Cimoli, Xiaozhou Ruan, Bryan Kaiser, and
777 Ryan Holmes for insightful discussions about abyssal mixing layers. We are grateful for two

778 reviewers whose feedback improved the manuscript. We acknowledge funding support from Na-
779 tional Science Foundation awards 6932401 and 6936732.

780 **References**

781 Abernathey, R., D. Ferreira, and A. Klocker, 2013: Diagnostics of isopycnal mixing in a cir-
782 cumpolar channel. *Ocean Modelling*, **72**, 1–16, doi:10.1016/j.ocemod.2013.07.004, URL [http://](http://www.sciencedirect.com/science/article/pii/S1463500313001200)
783 www.sciencedirect.com/science/article/pii/S1463500313001200.

784 Abernathey, R. P., I. Cerovecki, P. R. Holland, E. Newsom, M. Mazloff, and L. D. Talley, 2016:
785 Water-mass transformation by sea ice in the upper branch of the Southern Ocean overturn-
786 ing. *Nature Geoscience*, **9 (8)**, 596–601, doi:10.1038/ngeo2749, URL [http://www.nature.com/](http://www.nature.com/articles/ngeo2749)
787 [articles/ngeo2749](http://www.nature.com/articles/ngeo2749), publisher: Nature Publishing Group.

788 Archer, D., H. Kheshgi, and E. Maier-Reimer, 1998: Dynamics of fossil fuel CO₂ neutralization
789 by marine CaCO₃. *Global Biogeochemical Cycles*, **12 (2)**, 259–276, doi:10.1029/98GB00744,
790 URL <http://doi.wiley.com/10.1029/98GB00744>.

791 Bezanson, J., A. Edelman, S. Karpinski, and V. Shah, 2017: Julia: A Fresh Approach to Numerical
792 Computing. *SIAM Review*, **59 (1)**, 65–98, doi:10.1137/141000671, URL [https://epubs.siam.org/](https://epubs.siam.org/doi/10.1137/141000671)
793 [doi/10.1137/141000671](https://epubs.siam.org/doi/10.1137/141000671).

794 Bryan, K., and L. J. Lewis, 1979: A water mass model of the world ocean. *Journal of Geophysical*
795 *Research*, **84 (C5)**, 2503–2517, doi:10.1029/JC084iC05p02503, iSBN: 0148-0227.

796 Callies, J., 2018: Restratification of Abyssal Mixing Layers by Submesoscale Baroclinic Eddies.
797 *Journal of Physical Oceanography*, JPO–D–18–0082.1, doi:10.1175/JPO-D-18-0082.1, URL
798 <http://journals.ametsoc.org/doi/10.1175/JPO-D-18-0082.1>.

799 Callies, J., and R. Ferrari, 2018: Dynamics of an Abyssal Circulation Driven by Bottom-
800 Intensified Mixing on Slopes. *Journal of Physical Oceanography*, **48** (6), 1257–1282, doi:
801 10.1175/JPO-D-17-0125.1, URL <http://journals.ametsoc.org/doi/10.1175/JPO-D-17-0125.1>.

802 Cember, R. P., 1998: On deep western boundary currents. *Journal of Geophysical Research:*
803 *Oceans*, **103** (C3), 5397–5417, doi:10.1029/97JC02422, URL <https://agupubs.onlinelibrary.wiley.com/doi/abs/10.1029/97JC02422>.

804

805 Cimoli, L., C.-c. P. Caulfield, H. L. Johnson, D. P. Marshall, A. Mashayek, A. C. N. Garabato,
806 and C. Vic, 2019: Sensitivity of deep ocean mixing to local internal tide breaking and mixing
807 efficiency. *Geophysical Research Letters*, **n/a** (n/a), doi:10.1029/2019GL085056, URL <https://agupubs.onlinelibrary.wiley.com/doi/abs/10.1029/2019GL085056>.

808

809 de Lavergne, C., G. Madec, J. Le Sommer, A. J. G. Nurser, and A. C. Naveira Garabato, 2016a:
810 The Impact of a Variable Mixing Efficiency on the Abyssal Overturning. *Journal of Physical*
811 *Oceanography*, **46** (2), 663–681, doi:10.1175/JPO-D-14-0259.1, URL <http://journals.ametsoc.org/doi/10.1175/JPO-D-14-0259.1>.

812

813 de Lavergne, C., G. Madec, J. Le Sommer, A. J. G. Nurser, and A. C. Naveira Garabato, 2016b:
814 On the Consumption of Antarctic Bottom Water in the Abyssal Ocean. *Journal of Physical*
815 *Oceanography*, **46** (2), 635–661, doi:10.1175/JPO-D-14-0201.1, URL <http://journals.ametsoc.org/doi/10.1175/JPO-D-14-0201.1>.

816

817 de Lavergne, C., G. Madec, F. Roquet, R. M. Holmes, and T. J. McDougall, 2017: Abyssal
818 ocean overturning shaped by seafloor distribution. *Nature*, **551** (7679), 181–186, doi:10.1038/
819 nature24472, URL <http://www.nature.com/doi/10.1038/nature24472>, publisher: Nature
820 Publishing Group.

821 De Szoeké, R. A., and A. F. Bennett, 1993: Microstructure Fluxes across Density Surfaces. *Journal of Physical Oceanography*, **23** (10), 2254–2264, doi:10.1175/1520-0485(1993)023<2254:
822 MFADS>2.0.CO;2, URL [https://journals.ametsoc.org/doi/abs/10.1175/1520-0485\(1993\)023%](https://journals.ametsoc.org/doi/abs/10.1175/1520-0485(1993)023%3C2254:MFADS%3E2.0.CO%3B2)
823 [3C2254:MFADS%3E2.0.CO%3B2](https://journals.ametsoc.org/doi/abs/10.1175/1520-0485(1993)023%3C2254:MFADS%3E2.0.CO%3B2), publisher: American Meteorological Society.

825 Dell, R., and L. Pratt, 2015: Diffusive boundary layers over varying topography. *Journal of Fluid*
826 *Mechanics*, **769**, 635–653, doi:10.1017/jfm.2015.88, URL [http://www.journals.cambridge.org/](http://www.journals.cambridge.org/abstract_S0022112015000889)
827 [abstract_S0022112015000889](http://www.journals.cambridge.org/abstract_S0022112015000889).

828 Drake, H., 2020: hdrake/abyssalflow: First set of revisions. Zenodo, URL [https://doi.org/10.5281/](https://doi.org/10.5281/zenodo.3746882)
829 [zenodo.3746882](https://doi.org/10.5281/zenodo.3746882), doi:10.5281/zenodo.3746882.

830 Emile-Geay, J., and G. Madec, 2009: Geothermal heating, diapycnal mixing and the abyssal circu-
831 lation. *Ocean Science*, **5** (2), 203–217, doi:10.5194/os-5-203-2009, URL [http://www.ocean-sci.](http://www.ocean-sci.net/5/203/2009/)
832 [net/5/203/2009/](http://www.ocean-sci.net/5/203/2009/).

833 Ferrari, R., A. Mashayek, T. J. McDougall, M. Nikurashin, and J.-M. Campin, 2016: Turning
834 Ocean Mixing Upside Down. *Journal of Physical Oceanography*, **46** (7), 2239–2261, doi:10.
835 1175/JPO-D-15-0244.1, URL <http://journals.ametsoc.org/doi/10.1175/JPO-D-15-0244.1>.

836 Garabato, A. C. N., and Coauthors, 2019: Rapid mixing and exchange of deep-ocean wa-
837 ters in an abyssal boundary current. *Proceedings of the National Academy of Sciences*,
838 **116** (27), 13 233–13 238, doi:10.1073/pnas.1904087116, URL [https://www.pnas.org/content/](https://www.pnas.org/content/116/27/13233)
839 [116/27/13233](https://www.pnas.org/content/116/27/13233), iISBN: 9781904087113 Publisher: National Academy of Sciences Section: Phys-
840 ical Sciences.

841 Garrett, C., 1990: The role of secondary circulation in boundary mixing. *Journal of Geophysical*
842 *Research*, **95** (C3), 3181, doi:10.1029/JC095iC03p03181, URL <http://doi.wiley.com/10.1029/>

843 JC095iC03p03181, publisher: Wiley-Blackwell.

844 Garrett, C., P. MacCready, and P. Rhines, 1993: Boundary Mixing and Arrested Ekman Layers:
845 Rotating Stratified Flow Near a Sloping Boundary. *Annual Review of Fluid Mechanics*, **25** (1),
846 291–323, doi:10.1146/annurev.fl.25.010193.001451, URL [http://www.annualreviews.org/doi/](http://www.annualreviews.org/doi/10.1146/annurev.fl.25.010193.001451)
847 [10.1146/annurev.fl.25.010193.001451](http://www.annualreviews.org/doi/10.1146/annurev.fl.25.010193.001451), publisher: Annual Reviews 4139 El Camino Way, P.O.
848 Box 10139, Palo Alto, CA 94303-0139, USA.

849 Gent, P. R., and J. C. McWilliams, 1990: Isopycnal Mixing in Ocean Circulation Models.
850 *Journal of Physical Oceanography*, **20** (1), 150–155, doi:10.1175/1520-0485(1990)020<0150:
851 IMIOCM>2.0.CO;2, URL [http://journals.ametsoc.org/doi/abs/10.1175/1520-0485\(1990\)020%](http://journals.ametsoc.org/doi/abs/10.1175/1520-0485(1990)020%3C0150:IMIOCM%3E2.0.CO;2)
852 [3C0150:IMIOCM%3E2.0.CO;2](http://journals.ametsoc.org/doi/abs/10.1175/1520-0485(1990)020%3C0150:IMIOCM%3E2.0.CO;2), iISBN: 0022-3670.

853 Gouretski, V., and K. P. Koltermann, 2004: WOCE global hydrographic climatology. *Berichte des*
854 *BSH*, **35**, 1–52.

855 Greatbatch, R. J., and K. G. Lamb, 1990: On Parameterizing Vertical Mixing of Momentum in
856 Non-eddy Resolving Ocean Models. *Journal of Physical Oceanography*, **20** (10), 1634–1637,
857 doi:10.1175/1520-0485(1990)020<1634:OPVMOM>2.0.CO;2, URL [https://journals.ametsoc.](https://journals.ametsoc.org/doi/abs/10.1175/1520-0485%281990%29020%3C1634%3AOPVMOM%3E2.0.CO%3B2)
858 [org/doi/abs/10.1175/1520-0485%281990%29020%3C1634%3AOPVMOM%3E2.0.CO%3B2](https://journals.ametsoc.org/doi/abs/10.1175/1520-0485%281990%29020%3C1634%3AOPVMOM%3E2.0.CO%3B2).

859 Gregg, M. C., 1989: Scaling turbulent dissipation in the thermocline. *Journal of Geophysical*
860 *Research*, **94** (C7), 9686, doi:10.1029/JC094iC07p09686, URL [http://doi.wiley.com/10.1029/](http://doi.wiley.com/10.1029/JC094iC07p09686)
861 [JC094iC07p09686](http://doi.wiley.com/10.1029/JC094iC07p09686).

862 Hansen, J., G. Russell, A. Lacis, I. Fung, D. Rind, and P. Stone, 1985: Climate Response Times:
863 Dependence on Climate Sensitivity and Ocean Mixing. *Science*, **229** (4716), 857–859, doi:

864 10.1126/science.229.4716.857, URL [http://www.sciencemag.org/cgi/doi/10.1126/science.229.](http://www.sciencemag.org/cgi/doi/10.1126/science.229.4716.857)
865 4716.857.

866 Hogg, N., P. Biscaye, W. Gardner, and W. Jr, 1982: On the Transport and Modification of Antarctic
867 Bottom Water in the Vema Channel. *J. Mar. Res.*, **40**, 231–263.

868 Holden, P. B., N. R. Edwards, K. Fraedrich, E. Kirk, F. Lunkeit, and X. Zhu, 2016:
869 PLASIMGENIE v1.0: a new intermediate complexity AOGCM. *Geoscientific Model Devel-*
870 *opment*, **9** (9), 3347–3361, doi:<https://doi.org/10.5194/gmd-9-3347-2016>, URL [https://www.](https://www.geosci-model-dev.net/9/3347/2016/)
871 [geosci-model-dev.net/9/3347/2016/](https://www.geosci-model-dev.net/9/3347/2016/).

872 Holmes, R. M., C. de Lavergne, and T. J. McDougall, 2018: Ridges, Seamounts, Troughs, and
873 Bowls: Topographic Control of the Dianeutral Circulation in the Abyssal Ocean. *Journal of*
874 *Physical Oceanography*, **48** (4), 861–882, doi:10.1175/JPO-D-17-0141.1, URL [http://journals.](http://journals.ametsoc.org/doi/10.1175/JPO-D-17-0141.1)
875 [ametsoc.org/doi/10.1175/JPO-D-17-0141.1](http://journals.ametsoc.org/doi/10.1175/JPO-D-17-0141.1).

876 Holmes, R. M., C. de Lavergne, and T. J. McDougall, 2019: Tracer Transport within
877 Abyssal Mixing Layers. *Journal of Physical Oceanography*, **49** (10), 2669–2695, doi:10.1175/
878 JPO-D-19-0006.1, URL <https://journals.ametsoc.org/doi/full/10.1175/JPO-D-19-0006.1>, pub-
879 lisher: American Meteorological Society.

880 Huang, R. X., and X. Jin, 2002: Deep Circulation in the South Atlantic Induced by Bottom-
881 Intensified Mixing over the Midocean Ridge*. *Journal of Physical Oceanography*, **32** (4), 1150–
882 1164, doi:10.1175/1520-0485(2002)032<1150:DCITSA>2.0.CO;2.

883 Jansen, M. F., and L.-P. Nadeau, 2019: A Toy Model for the Response of the Residual Overturning
884 Circulation to Surface Warming. *Journal of Physical Oceanography*, **49** (5), 1249–1268, doi:

885 10.1175/JPO-D-18-0187.1, URL <https://journals.ametsoc.org/doi/10.1175/JPO-D-18-0187.1>,
886 publisher: American Meteorological Society.

887 Jayne, S. R., 2009: The Impact of Abyssal Mixing Parameterizations in an Ocean General Circula-
888 tion Model. *Journal of Physical Oceanography*, **39** (7), 1756–1775, doi:10.1175/2009JPO4085.
889 1.

890 Kawase, M., 1987: Establishment of Deep Ocean Circulation Driven by Deep-Water Produc-
891 tion. *Journal of Physical Oceanography*, **17** (12), 2294–2317, doi:10.1175/1520-0485(1987)
892 017<2294:EODOCD>2.0.CO;2.

893 Koltermann, K. P., V. Gouretski, and K. Jancke, 2011: *Hydrographic Atlas of the World Ocean*
894 *Circulation Experiment (WOCE): Volume 3: Atlantic Ocean*. National Oceanography Centre.

895 Ledwell, J. R., E. T. Montgomery, K. L. Polzin, L. C. St. Laurent, R. W. Schmitt, and J. M.
896 Toole, 2000: Evidence for enhanced mixing over rough topography in the abyssal ocean. *Nature*,
897 **403** (6766), 179–182, doi:10.1038/35003164, URL <http://www.nature.com/articles/35003164>,
898 publisher: Nature Publishing Group.

899 Ledwell, J. R., A. J. Watson, and C. S. Law, 1993: Evidence for slow mixing across the py-
900 cnocline from an open-ocean tracer-release experiment. *Nature*, **364** (6439), 701–703, doi:
901 10.1038/364701a0, URL <http://www.nature.com/doi/10.1038/364701a0>, publisher: Na-
902 ture Publishing Group.

903 Lumpkin, R., and K. Speer, 2007: Global Ocean Meridional Overturning. *Journal of Physical*
904 *Oceanography*, **37** (10), 2550–2562, doi:10.1175/JPO3130.1, URL [http://dx.doi.org/10.1175/](http://dx.doi.org/10.1175/JPO3130.1)
905 [JPO3130.1](http://dx.doi.org/10.1175/JPO3130.1), ISBN: 0022-3670.

906 MacKinnon, J. A., and Coauthors, 2017: Climate Process Team on Internal WaveDriven Ocean
907 Mixing. *Bulletin of the American Meteorological Society*, **98 (11)**, 2429–2454, doi:10.1175/
908 BAMS-D-16-0030.1, URL <http://journals.ametsoc.org/doi/10.1175/BAMS-D-16-0030.1>.

909 Marotzke, J., 1997: Boundary Mixing and the Dynamics of Three-Dimensional Thermo-
910 haline Circulations. *Journal of Physical Oceanography*, **27 (8)**, 1713–1728, doi:10.1175/
911 1520-0485(1997)027<1713:BMATDO>2.0.CO;2, URL <https://journals.ametsoc.org/doi/full/10.1175/1520-0485%281997%29027%3C1713%3ABMATDO%3E2.0.CO%3B2>.

913 Marshall, J., D. Jamous, and J. Nilsson, 1999: Reconciling thermodynamic and dynamic methods
914 of computation of water-mass transformation rates. *Deep-Sea Research Part I: Oceanographic
915 Research Papers*, **46 (4)**, 545–572, doi:10.1016/S0967-0637(98)00082-X, iSBN: 0967-0637.

916 Marshall, J., and T. Radko, 2003: Residual-Mean Solutions for the Antarctic Circumpolar Current
917 and Its Associated Overturning Circulation. *Journal of Physical Oceanography*, **33 (11)**, 2341–
918 2354, doi:10.1175/1520-0485(2003)033<2341:RSFTAC>2.0.CO;2, URL [http://dx.doi.org/10.1175/1520-0485\(2003\)033%3C2341:RSFTAC%3E2.0.CO;2](http://dx.doi.org/10.1175/1520-0485(2003)033%3C2341:RSFTAC%3E2.0.CO;2), iSBN: 0022-3670.

920 Marshall, J., and K. Speer, 2012: Closure of the meridional overturning circulation through
921 Southern Ocean upwelling. *Nature Geoscience*, **5 (3)**, 171–180, doi:10.1038/ngeo1391, URL
922 <http://dx.doi.org/10.1038/ngeo1391>, publisher: Nature Publishing Group iSBN: 1752-0894.

923 McDougall, T. J., and R. Ferrari, 2017: Abyssal Upwelling and Downwelling Driven by
924 Near-Boundary Mixing. *Journal of Physical Oceanography*, **47 (2)**, 261–283, doi:10.1175/
925 JPO-D-16-0082.1, URL <https://journals.ametsoc.org/doi/full/10.1175/JPO-D-16-0082.1>, pub-
926 lisher: American Meteorological Society.

927 Melet, A., S. Legg, and R. Hallberg, 2016: Climatic Impacts of Parameterized Local and Remote
928 Tidal Mixing. *Journal of Climate*, **29** (10), 3473–3500, doi:10.1175/JCLI-D-15-0153.1, URL
929 <http://journals.ametsoc.org/doi/10.1175/JCLI-D-15-0153.1>.

930 Munk, W. H., 1966: Abyssal recipes. *Deep Sea Research and Oceanographic Abstracts*, **13** (4),
931 707–730, doi:10.1016/0011-7471(66)90602-4, arXiv: cs/9605103 ISBN: 1600117471.

932 Munk, W. H., and C. Wunsch, 1998: Abyssal Recipes II: energetics of tidal and wind mixing.
933 *Deep-Sea Research Part I: Oceanographic Research Papers*, **45**, 1978–2010.

934 Nikurashin, M., and R. Ferrari, 2009: Radiation and Dissipation of Internal Waves Generated
935 by Geostrophic Motions Impinging on Small-Scale Topography: Theory. *Journal of Phys-*
936 *ical Oceanography*, **40** (5), 1055–1074, doi:10.1175/2009JPO4199.1, URL [https://journals.](https://journals.ametsoc.org/doi/full/10.1175/2009JPO4199.1)
937 [ametsoc.org/doi/full/10.1175/2009JPO4199.1](https://journals.ametsoc.org/doi/full/10.1175/2009JPO4199.1).

938 Nikurashin, M., and R. Ferrari, 2011: Global energy conversion rate from geostrophic
939 flows into internal lee waves in the deep ocean. *Geophysical Research Letters*, **38** (8),
940 doi:10.1029/2011GL046576, URL [https://agupubs.onlinelibrary.wiley.com/doi/abs/10.1029/](https://agupubs.onlinelibrary.wiley.com/doi/abs/10.1029/2011GL046576)
941 [2011GL046576](https://agupubs.onlinelibrary.wiley.com/doi/abs/10.1029/2011GL046576).

942 Nikurashin, M., and R. Ferrari, 2013: Overturning circulation driven by breaking internal waves
943 in the deep ocean. *Geophysical Research Letters*, **40** (12), 3133–3137, doi:10.1002/grl.50542,
944 URL <http://doi.wiley.com/10.1002/grl.50542>, publisher: Wiley-Blackwell.

945 Nikurashin, M., and S. Legg, 2011: A Mechanism for Local Dissipation of Internal Tides
946 Generated at Rough Topography. *Journal of Physical Oceanography*, **41** (2), 378–395, doi:
947 [10.1175/2010JPO4522.1](http://journals.ametsoc.org/doi/abs/10.1175/2010JPO4522.1), URL <http://journals.ametsoc.org/doi/abs/10.1175/2010JPO4522.1>.

948 Nikurashin, M., and G. Vallis, 2011: A Theory of Deep Stratification and Overturning Circulation
949 in the Ocean. *Journal of Physical Oceanography*, **41** (3), 485–502, doi:10.1175/2010JPO4529.
950 1, URL <http://journals.ametsoc.org/doi/abs/10.1175/2010JPO4529.1>.

951 Nikurashin, M., G. Vallis, M. Nikurashin, and G. Vallis, 2012: A Theory of the Interhemispheric
952 Meridional Overturning Circulation and Associated Stratification. *Journal of Physical Oceanog-*
953 *raphy*, **42** (10), 1652–1667, doi:10.1175/JPO-D-11-0189.1, URL [http://journals.ametsoc.org/](http://journals.ametsoc.org/doi/abs/10.1175/JPO-D-11-0189.1)
954 [doi/abs/10.1175/JPO-D-11-0189.1](http://journals.ametsoc.org/doi/abs/10.1175/JPO-D-11-0189.1).

955 Nycander, J., 2005: Generation of internal waves in the deep ocean by tides. *Journal of Geo-*
956 *physical Research: Oceans*, **110** (C10), doi:10.1029/2004JC002487, URL [https://agupubs.](https://agupubs.onlinelibrary.wiley.com/doi/abs/10.1029/2004JC002487)
957 [onlinelibrary.wiley.com/doi/abs/10.1029/2004JC002487](https://agupubs.onlinelibrary.wiley.com/doi/abs/10.1029/2004JC002487).

958 Osborn, T. R., 1980: Estimates of the Local Rate of Vertical Diffusion from Dissipation Mea-
959 surements. *Journal of Physical Oceanography*, **10** (1), 83–89, doi:10.1175/1520-0485(1980)
960 010(0083:EOTLRO)2.0.CO;2, URL [http://journals.ametsoc.org/doi/abs/10.1175/1520-0485%](http://journals.ametsoc.org/doi/abs/10.1175/1520-0485%281980%29010%3C0083%3AEOTLRO%3E2.0.CO%3B2)
961 [281980%29010%3C0083%3AEOTLRO%3E2.0.CO%3B2](http://journals.ametsoc.org/doi/abs/10.1175/1520-0485%281980%29010%3C0083%3AEOTLRO%3E2.0.CO%3B2).

962 Pedlosky, J., 1992: The Baroclinic Structure of the Abyssal Circulation. *Journal of Physical*
963 *Oceanography*, **22** (6), 652–659, doi:10.1175/1520-0485(1992)022<0652:TBSOTA>2.0.CO;2.

964 Pedlosky, J., 1996: *Ocean Circulation Theory*. Springer Berlin Heidelberg, Berlin, Heidelberg,
965 doi:10.1007/978-3-662-03204-6, URL <http://link.springer.com/10.1007/978-3-662-03204-6>.

966 Phillips, O., 1970: On flows induced by diffusion in a stably stratified fluid. *Deep Sea Research and*
967 *Oceanographic Abstracts*, **17** (3), 435–443, doi:10.1016/0011-7471(70)90058-6, URL [http://](http://linkinghub.elsevier.com/retrieve/pii/0011747170900586)
968 linkinghub.elsevier.com/retrieve/pii/0011747170900586.

- 969 Phillips, O. M., J.-H. Shyu, and H. Salmun, 1986: An experiment on boundary mixing: mean
970 circulation and transport rates. *Journal of Fluid Mechanics*, **173** (-1), 473, doi:10.1017/
971 S0022112086001234, URL http://www.journals.cambridge.org/abstract_S0022112086001234.
- 972 Polzin, K., J. Toole, J. R. Ledwell, and R. Schmitt, 1997: Spatial Variability of Turbulent Mix-
973 ing in the Spatial Variability Abyssal Ocean. *Science*, **276** (5309), 93–96, doi:10.1126/science.
974 276.5309.93, URL <http://www.sciencemag.org/cgi/content/abstract/276/5309/93>, iSBN: 0036-
975 8075.
- 976 Polzin, K. L., 2009: An abyssal recipe. *Ocean Modelling*, **30** (4), 298–309, doi:10.1016/j.ocemod.
977 2009.07.006.
- 978 Rhines, P. B., 1993: Oceanic General Circulation: Wave and Advection Dynamics. *Modelling*
979 *Oceanic Climate Interactions*, J. Willebrand, and D. L. T. Anderson, Eds., Springer Berlin Hei-
980 delberg, Berlin, Heidelberg, 67–149.
- 981 Robinson, A., and H. Stommel, 1959: The Oceanic Thermocline and the Associated Thermo-
982 haline Circulation. *Tellus*, **11** (3), 295–308, doi:10.1111/j.2153-3490.1959.tb00035.x, URL
983 <http://tellusa.net/index.php/tellusa/article/view/9317>, publisher: Wiley/Blackwell (10.1111).
- 984 Salmon, R., 1992: A two-layer Gulf Stream over a continental slope. *Journal of Marine Research*,
985 **50** (3), 341–365, doi:10.1357/002224092784797610, URL [http://openurl.ingenta.com/content/
986 xref?genre=article&issn=0022-2402&volume=50&issue=3&spage=341](http://openurl.ingenta.com/content/xref?genre=article&issn=0022-2402&volume=50&issue=3&spage=341).
- 987 Salmun, H., P. D. Killworth, and J. R. Blundell, 1991: A two-dimensional model of boundary
988 mixing. *Journal of Geophysical Research: Oceans*, **96** (C10), 18 447–18 474, doi:10.1029/
989 91JC01917, URL <https://agupubs.onlinelibrary.wiley.com/doi/abs/10.1029/91JC01917>.

- 990 Samelson, R. M., 1998: Large-Scale Circulation with Locally Enhanced Vertical Mixing*.
991 *Journal of Physical Oceanography*, **28** (4), 712–726, doi:10.1175/1520-0485(1998)028<0712:
992 LSCWLE>2.0.CO;2, URL [http://journals.ametsoc.org/doi/abs/10.1175/1520-0485%281998%](http://journals.ametsoc.org/doi/abs/10.1175/1520-0485%281998%29028%3C0712%3ALSCWLE%3E2.0.CO%3B2)
993 [29028%3C0712%3ALSCWLE%3E2.0.CO%3B2](http://journals.ametsoc.org/doi/abs/10.1175/1520-0485%281998%29028%3C0712%3ALSCWLE%3E2.0.CO%3B2).
- 994 Sarmiento, J. L., and J. R. Toggweiler, 1984: A new model for the role of the oceans in determining
995 atmospheric PCO₂. *Nature*, **308** (5960), 621–624, doi:10.1038/308621a0, URL [http://www.](http://www.nature.com/doi/abs/10.1038/308621a0)
996 [nature.com/doi/abs/10.1038/308621a0](http://www.nature.com/doi/abs/10.1038/308621a0), publisher: Nature Publishing Group.
- 997 Sheen, K. L., and Coauthors, 2013: Rates and mechanisms of turbulent dissipation and mixing
998 in the Southern Ocean: Results from the Diapycnal and Isopycnal Mixing Experiment in the
999 Southern Ocean (DIMES). *Journal of Geophysical Research: Oceans*, **118** (6), 2774–2792, doi:
1000 10.1002/jgrc.20217, URL <https://agupubs.onlinelibrary.wiley.com/doi/abs/10.1002/jgrc.20217>,
1001 [_eprint: https://agupubs.onlinelibrary.wiley.com/doi/pdf/10.1002/jgrc.20217](https://agupubs.onlinelibrary.wiley.com/doi/pdf/10.1002/jgrc.20217).
- 1002 St. Laurent, L., and C. Garrett, 2002: The Role of Internal Tides in Mixing the Deep
1003 Ocean. *Journal of Physical Oceanography*, **32** (10), 2882–2899, doi:10.1175/1520-0485(2002)
1004 032<2882:TROITI>2.0.CO;2, URL [http://journals.ametsoc.org/doi/abs/10.1175/1520-0485%](http://journals.ametsoc.org/doi/abs/10.1175/1520-0485%282002%29032%3C2882%3ATROITI%3E2.0.CO%3B2)
1005 [282002%29032%3C2882%3ATROITI%3E2.0.CO%3B2](http://journals.ametsoc.org/doi/abs/10.1175/1520-0485%282002%29032%3C2882%3ATROITI%3E2.0.CO%3B2).
- 1006 St. Laurent, L. C., J. M. Toole, and R. W. Schmitt, 2001: Buoyancy Forcing by Turbulence above
1007 Rough Topography in the Abyssal Brazil Basin*. *Journal of Physical Oceanography*, **31** (12),
1008 3476–3495, doi:10.1175/1520-0485(2001)031<3476:BFBTAR>2.0.CO;2.
- 1009 Stommel, H., 1948: The westward intensification of wind-driven ocean currents. *Transactions,*
1010 *American Geophysical Union*, **29** (2), 202, doi:10.1029/TR029i002p00202, URL [http://doi.](http://doi.wiley.com/10.1029/TR029i002p00202)
1011 [wiley.com/10.1029/TR029i002p00202](http://doi.wiley.com/10.1029/TR029i002p00202).

- 1012 Stommel, H., 1957: The Abyssal Circulation of the Ocean. *Nature*, **180 (4589)**, 733–734, doi:
1013 10.1038/180733a0, URL <http://www.nature.com/doi/10.1038/180733a0>.
- 1014 Stommel, H., and A. B. Arons, 1959a: On the abyssal circulation of the world ocean II. An
1015 idealized model of the circulation pattern and amplitude in oceanic basins. *Deep Sea Research*
1016 (1953), **6**, 217–233, doi:10.1016/0146-6313(59)90075-9, URL [http://www.sciencedirect.com/
1017 science/article/pii/0146631359900759](http://www.sciencedirect.com/science/article/pii/0146631359900759).
- 1018 Stommel, H., and A. B. Arons, 1959b: On the abyssal circulation of the world ocean I.
1019 Stationary planetary flow patterns on a sphere. *Deep Sea Research (1953)*, **6**, 140–
1020 154, doi:10.1016/0146-6313(59)90065-6, URL [http://www.sciencedirect.com/science/article/
1021 pii/0146631359900656](http://www.sciencedirect.com/science/article/pii/0146631359900656).
- 1022 Sverdrup, H., M. Johnson, and R. Fleming, 1942: The Oceans: Their Physics, Chemistry
1023 and General Biology. *Oceanography*, 1104, doi:10.2307/210609, arXiv: 1011.1669v3 ISBN:
1024 9788578110796.
- 1025 Talley, L. D., 2007: *Hydrographic atlas of the world ocean circulation experiment (WOCE): Vol-*
1026 *ume 2: Pacific Ocean*. WOCE International Project Office Southampton.
- 1027 Talley, L. D., 2013a: Closure of the Global Overturning Circulation Through the Indian, Pacific,
1028 and Southern Oceans: Schematics and Transports. *Oceanography*, **26 (1)**, 80–97, doi:10.
1029 5670/oceanog.2013.07, URL [http://apps.webofknowledge.com/full_record.do?product=UA&
1030 search_mode=GeneralSearch&qid=14&SID=W1jPgX8kkS6brME6NvD&page=1&doc=1](http://apps.webofknowledge.com/full_record.do?product=UA&search_mode=GeneralSearch&qid=14&SID=W1jPgX8kkS6brME6NvD&page=1&doc=1),
1031 arXiv: 1011.1669v3 ISBN: 1042-8275.
- 1032 Talley, L. D., 2013b: *Hydrographic Atlas of the World Ocean Circulation Experiment (WOCE):*
1033 *volume 4: Indian Ocean*. International WOCE Project Office.

- 1034 Thompson, A. F., A. L. Stewart, and T. Bischoff, 2016: A Multibasin Residual-Mean Model for
1035 the Global Overturning Circulation. *Journal of Physical Oceanography*, **46** (9), 2583–2604, doi:
1036 10.1175/JPO-D-15-0204.1, URL <http://journals.ametsoc.org/doi/10.1175/JPO-D-15-0204.1>.
- 1037 Thompson, L., and G. C. Johnson, 1996: Abyssal currents generated by diffusion and geothermal
1038 heating over rises. *Deep Sea Research Part I: Oceanographic Research Papers*, **43** (2), 193–
1039 211, doi:10.1016/0967-0637(96)00095-7, URL [http://www.sciencedirect.com/science/article/
1040 pii/0967063796000957](http://www.sciencedirect.com/science/article/pii/0967063796000957).
- 1041 Thorpe, S. A., 1987: Current and Temperature Variability on the Continental Slope. *Philosophical
1042 Transactions of the Royal Society A: Mathematical, Physical and Engineering Sciences*,
1043 **323** (1574), 471–517, doi:10.1098/rsta.1987.0100, URL [http://rsta.royalsocietypublishing.org/
1044 cgi/doi/10.1098/rsta.1987.0100](http://rsta.royalsocietypublishing.org/cgi/doi/10.1098/rsta.1987.0100), publisher: The Royal Society.
- 1045 Thurnherr, A. M., and K. G. Speer, 2003: Boundary Mixing and Topographic Blocking on the
1046 Mid-Atlantic Ridge in the South Atlantic*. *Journal of Physical Oceanography*, **33** (4), 848–
1047 862, doi:10.1175/1520-0485(2003)33<848:BMATBO>2.0.CO;2, URL [http://journals.ametsoc.
1048 org/doi/abs/10.1175/1520-0485%282003%2933%3C848%3ABMATBO%3E2.0.CO%3B2](http://journals.ametsoc.org/doi/abs/10.1175/1520-0485%282003%2933%3C848%3ABMATBO%3E2.0.CO%3B2).
- 1049 Thurnherr, A. M., and Coauthors, 2005: Mixing Associated with Sills in a Canyon on the Mi-
1050 docean Ridge Flank*. *Journal of Physical Oceanography*, **35** (8), 1370–1381, doi:10.1175/
1051 JPO2773.1, URL <http://journals.ametsoc.org/doi/abs/10.1175/JPO2773.1>.
- 1052 Toggweiler, J. R., K. Dixon, and K. Bryan, 1989: Simulations of radiocarbon in a coarse-
1053 resolution world ocean model: 1. Steady state prebomb distributions. *Journal of Geophysical
1054 Research*, **94** (C6), 8217, doi:10.1029/JC094iC06p08217, URL [http://doi.wiley.com/10.1029/
1055 JC094iC06p08217](http://doi.wiley.com/10.1029/JC094iC06p08217).

- 1056 Walin, G., 1982: On the relation between sea-surface heat flow and thermal circulation in the
1057 ocean. *Tellus*, **34** (2), 187–195, doi:10.3402/tellusa.v34i2.10801, URL [https://doi.org/10.3402/
1058 tellusa.v34i2.10801](https://doi.org/10.3402/tellusa.v34i2.10801).
- 1059 Waterhouse, A. F., and Coauthors, 2014: Global Patterns of Diapycnal Mixing from Measurements
1060 of the Turbulent Dissipation Rate. *Journal of Physical Oceanography*, **44** (7), 1854–1872, doi:
1061 10.1175/JPO-D-13-0104.1, URL [http://journals.ametsoc.org/doi/abs/10.1175/JPO-D-13-0104.
1062 1](http://journals.ametsoc.org/doi/abs/10.1175/JPO-D-13-0104.1), iISBN: 0022-3670.
- 1063 Wenegrat, J. O., J. Callies, and L. N. Thomas, 2018: Submesoscale Baroclinic Instability in the
1064 Bottom Boundary Layer. *Journal of Physical Oceanography*, JPO–D–17–0264.1, doi:10.1175/
1065 JPO-D-17-0264.1, URL <http://journals.ametsoc.org/doi/10.1175/JPO-D-17-0264.1>.
- 1066 Wunsch, C., 1970: On oceanic boundary mixing. *Deep-Sea Research and Oceanographic Ab-*
1067 *stracts*, **17** (2), 293–301, doi:10.1016/0011-7471(70)90022-7.
- 1068 Young, W. R., 2011: An Exact Thickness-Weighted Average Formulation of the Boussinesq Equa-
1069 tions. *Journal of Physical Oceanography*, **42** (5), 692–707, doi:10.1175/JPO-D-11-0102.1,
1070 URL <https://journals.ametsoc.org/doi/full/10.1175/JPO-D-11-0102.1>.

LIST OF FIGURES

1071			
1072	Fig. 1.	Schematic of a basin-scale abyssal circulation driven by near-boundary mixing. Dense bot-	
1073		tom waters flow northward out of the Southern Ocean via a deep western boundary current	
1074		(red circle) along the smooth and relatively quiescent continental slope, where little water-	
1075		mass transformation occurs. A cross-basin zonal flow feeds bottom waters from the deep	
1076		western boundary current into a system of abyssal mixing layers driven by bottom-enhanced	
1077		turbulent mixing over the rough topography of the mid-ocean ridge flanks (squiggly orange	
1078		arrows). The turbulent buoyancy flux converges in a bottom boundary layer (BBL), driv-	
1079		ing vigorous diabatic upwelling across buoyancy surfaces (grey lines). In a stratified mixing	
1080		layer (SML) above, the buoyancy flux diverges, driving diabatic downwelling. The net effect	
1081		of the up- and down-welling in the abyssal mixing layers is a net transformation of bottom	
1082		waters into deep waters. The newly formed deep waters return via cross-basin zonal flows	
1083		to the smooth continental slope, wherein they flow southward in a deep western boundary	
1084		current (blue circles) to close the abyssal circulation in the Southern Ocean. For simplicity,	
1085		we omit the alternating along-ridge flows (see Figure 3b) that are in frictional thermal-wind	
1086		balance with the plunging isopycnals.	56
1087	Fig. 2.	Configuration of the Planetary Geostrophic Circulation Model (PGCM). (a) Seafloor depth	
1088		in the PGCM. We highlight the southern restoring region where we apply a buoyancy restor-	
1089		ing which acts to transform deep waters into bottom waters (see Section 3c) and a northern-	
1090		hemisphere region in which we diagnose watermass transformations along the mid-ocean	
1091		ridge (see Section 4c). (b) Zonal section of the imposed turbulent diffusivity κ , which is	
1092		bottom-enhanced over the mid-ocean ridge. (c) The red lines show the four stratification	
1093		profiles B_z used in the PGCM as both the initial condition and as the reference profile for	
1094		buoyancy restoring in the southern restoring region. The black line shows the observed strat-	
1095		ification profile from the World Ocean Circulation Experiment (Gouretski and Koltermann	
1096		2004) in the South Pacific, averaged horizontally from 55°S to 45°S and 175°E to 115°W.	57
1097	Fig. 3.	Cartesian components of the velocity vector in the PGCM-REAL simulation along: (a-c)	
1098		a mid-latitude section in the northern hemisphere, $y = 3000$ km, and (d-f) a section at the	
1099		equator, $y = 0$ km. Black lines show three equally spaced buoyancy surfaces.	58
1100	Fig. 4.	(a) Barotropic, (b) meridional, and (c) zonal overturning circulations in the PGCM-REAL	
1101		simulation (see definitions in Section 4b). In all cases, positive values (red) correspond to	
1102		counter-clockwise circulations. The blue and red solid lines in (b) and (c), respectively,	
1103		show the height of the mid-ocean ridge along the dashed lines of the same colors in (a).	
1104		The thick black lines in (a) are the 3000 m and 4000 m isobaths, which highlight both the	
1105		continental slopes and the mid-ocean ridge. The thin black lines in (b) and (c) are equally-	
1106		spaced buoyancy surfaces, sampled at $x = L/4$ and $y = L/2$, respectively.	59
1107	Fig. 5.	Watermass transformations from the PGCM-REAL simulation in (a) the full northern hemi-	
1108		sphere basin ($y > 0$), (b) along the northern-hemisphere mid-ocean ridge ($y > 0, L/2 < x <$	
1109		$3L/2$), and (c) in a limited watermass analysis region along the northern-hemisphere mid-	
1110		-ocean ridge ($0 < y < L/2, L/2 < x < 3L/2$), as highlighted in Figure 2. The black line shows	
1111		the net watermass transformation, defined by equation (18). The red and blue lines show the	
1112		contributions from the bottom boundary layer (BBL) and the stratified mixing layer above	
1113		(SML). The dashed lines show the contributions from only the vertical component of the	
1114		buoyancy flux. All watermass transformations in the paper are computed in buoyancy space	
1115		and remapped into depth space (according to eq. 19).	60
1116	Fig. 6.	Vertical velocity (colors) and buoyancy surfaces (black lines) in abyssal mixing layers along	
1117		a zonal section across the mid-ocean ridge at $y = L/2$ in (a,c) the 1D PGCM emulator and	

1118 (b,d) the full 3D PGCM, where both are initialized from identical constant stratification
 1119 buoyancy fields. The top row shows the solutions at an initial time $\hat{t} = 0.1$, at which point the
 1120 abyssal mixing layers have spun up but the basin-scale circulation has not (see Section 3d).
 1121 The bottom row shows the solution at $\hat{t} = 50$, at which point the full solution has roughly
 1122 come to equilibrium with the buoyancy restoring in the Southern Ocean. The predicted
 1123 buoyancy surfaces in (a,c) are reproduced as dashed grey lines in (b,d) to show how the 1D
 1124 emulator predicts the buoyancy field well for short times but that the interior stratification in
 1125 the PGCM drifts far from the 1D emulator's prediction as it approaches equilibrium. 61

1126 **Fig. 7.** (a) Temporal evolution and (b,c) meridional structure of the stratification in PGCM simu-
 1127 lations. Grey-scale lines in (a) show the temporal evolution of the horizontal-mean strati-
 1128 fication in the Northern Hemisphere for simulations with a constant stratification restoring
 1129 buoyancy profile (solid lines) and a restoring buoyancy profile corresponding to stratification
 1130 that decays with depth with a scale height of $\delta = 1000$ m (dashed lines). The dashed brown
 1131 line delineates the height of the ridge crest. Panels (b) and (c) show the zonal-mean strati-
 1132 fication at equilibrium $\hat{t} = 50$ (colors) and equally-spaced buoyancy surfaces (black lines) for
 1133 experiments with restoring to constant and exponential stratification, respectively. 62

1134 **Fig. 8.** Watermass transformations in: (a, e) a 1D emulator of the PGCM and (b-d, f-h) the 3D
 1135 PGCM simulations with restoring buoyancy profiles corresponding to stratification profiles
 1136 with various exponential scale heights δ (we recover $N^2 = \text{constant}$ as $\delta \rightarrow \infty$). The initial
 1137 spin-up at $\hat{t} = 0.1$ is shown in (a-d) and the equilibrium state at $\hat{t} = 50$ is show in (e-h).
 1138 Black, red, and blue lines show the net, bottom boundary layer (BBL), and stratified mixing
 1139 layer (SML) contributions to the watermass transformations, respectively. The black dashed
 1140 line in (a,e) shows the integral constraint $L\Psi_\infty = L\kappa_{\text{bg}} \cot \theta_{\text{max}}$ derived from boundary layer
 1141 theory, where we take θ_{max} as the maximum slope angle of the mid-ocean ridge flank. 63

1142 **Fig. 9.** Scaling of watermass transformations in mixing layers with (a) the height δ over which the
 1143 restoring stratification varies and (b) the bottom diffusivity κ_{bot} . Colored symbols represent
 1144 the absolute value of the maximum transport in the BBL (red), the SML (blue), and the net
 1145 (black), with diamonds representing the PGCM-REAL simulations. The grey shading in
 1146 (a) represents realistic vertical scales δ over which abyssal stratification varies and in (b)
 1147 represents plausible values of the bottom diffusivity κ_{bot} . Panel (c) provides an example of
 1148 the watermass transformations for a bottom diffusivity $\kappa_{\text{bot}} = 5 \times 10^{-3} \text{ m}^2\text{s}^{-1}$, a stratification
 1149 height scale $\delta = 1000$ m, and a ridge height of $r_h = 1500$ m, where the corresponding
 1150 maxima are marked by diamonds and the dashed brown line represents the ridge crest. In all
 1151 experiments, the maximum net and BBL transformations occur at depths of roughly 4250 m,
 1152 at the base of the ridge slope, while the maximum SML transformation occurs at the ridge
 1153 crest. 64

1154 **Fig. 10.** Watermass transformations in PGCM simulations as a function of ridge height. All panels
 1155 are for a fixed constant stratification restoring buoyancy profile. The initial spin-up at $\hat{t} = 0.1$
 1156 is shown in (a-d) and the equilibrium state at $\hat{t} = 50$ is shown in (e-h). Mid-ocean ridge height
 1157 increases in increments of 500 m from left to right, as indicated by the dashed brown lines.
 1158 Black, red, and blue lines show the net, bottom boundary layer (BBL), and stratified mixing
 1159 layer (SML) contributions to the watermass transformations, respectively. 65

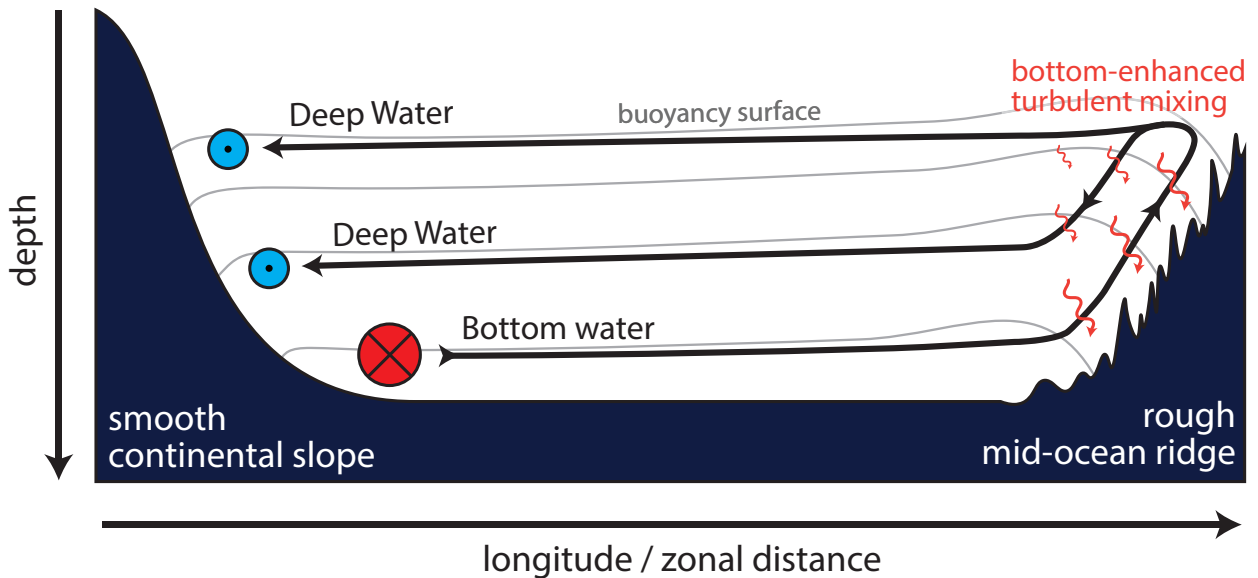
1160 **Fig. 11.** Diabatic zonal overturning circulation driven by bottom-enhanced mixing on the western
 1161 flank of a mid-ocean ridge in (a) the South Atlantic Ocean and (b) the western half of
 1162 the PGCM-REAL simulation domain. White lines show arbitrarily chosen contours of the
 1163 counter-clockwise zonal overturning streamfunction, where the values for (a) are digitized
 1164 from Figure 14 of St. Laurent et al. (2001) and for (b) are diagnosed from PGCM-REAL
 1165 simulation. Coloring shows the vertical diffusivity in log-scale (light-grey shading repre-

1166 sents depths with no microstructure measurements and does not necessarily represent to-
 1167 pography), where panel (a) is inspired by Figure 2 of Polzin et al. (1997) and the diffusivity
 1168 is calculated with microstructure profiles from the BBTRE experiment (Polzin et al. 1997;
 1169 St. Laurent et al. 2001, archived at microstructure.ucsd.edu). Black lines are: (a) poten-
 1170 tial density σ_4 surfaces (referenced to 4000 m) from the microstructure profiles and (b)
 1171 buoyancy surfaces from the PGCM solution, chosen arbitrarily to show that the zonal over-
 1172 turning circulation is indeed diabatic. The dark grey lines in (a) show the depth minimum
 1173 (canyon thalweg) and maximum (canyon crest) seafloor depth within 0.5° latitude of the
 1174 microstructure profiles. In (b), zonal distance along the PGCM section has been converted
 1175 to an equivalent longitude at 25°S so that length scales can be directly compared between
 1176 the two panels. 66

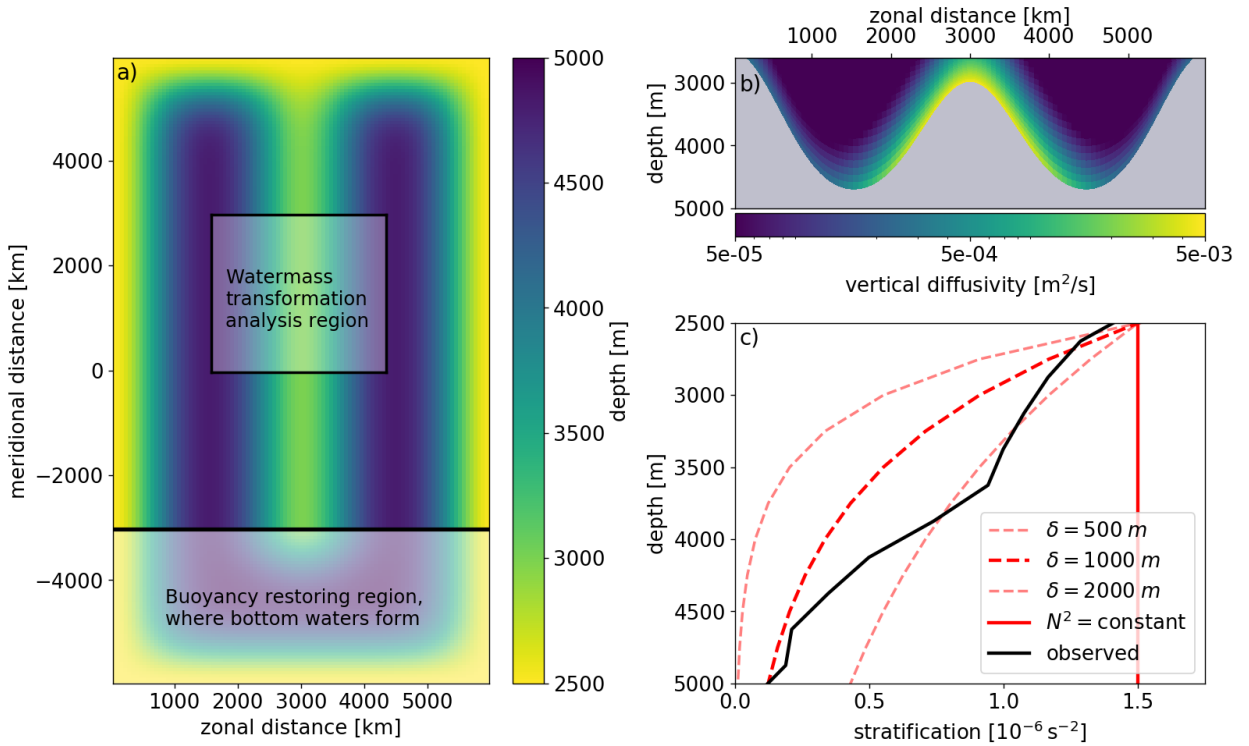
1177 **Fig. 12.** (a-d) Watermass transformations at all abyssal depths and (e,f) buoyancy flux convergence
 1178 at 3250 m depth in similarly-sized domains containing mid-ocean ridges, as diagnosed from
 1179 (a,e) the PGCM-REAL simulation and estimated for the (b,f) Pacific, (c,f) Atlantic, and
 1180 (d,f) Indian Oceans. In (a-d), the black, red, and blue lines show the net, bottom boundary
 1181 layer (BBL), and stratified mixing layer (SML) contributions to the watermass transfor-
 1182 mations, respectively (grey shaded indicates depths representing very little ocean volume). The
 1183 black boxes in (e,f) delineate the similarly-sized regions (each with dimensions of roughly
 1184 $3000\text{ km} \times 3000\text{ km}$) for which we compute the watermass transformations. In (e,f), red and
 1185 blue show regions of buoyancy flux convergence (positive buoyancy tendency) and buoy-
 1186 ancy flux divergence (negative buoyancy tendency), respectively. 67

1187 **Fig. 13.** Comparison of abyssal upwelling diagnostics in the PGCM-REAL simulation for the water-
 1188 mass transformation analysis region highlighted in Figure 2a. The orange and blue lines in
 1189 panel (d) represent the left- and right-hand sides, respectively, of the horizontally-averaged
 1190 advection-diffusion balance $\langle w \rangle A \simeq \langle N^2 \rangle^{-1} \frac{d}{dz} [A(z) \langle \kappa \rangle \langle N^2 \rangle]$ (eq. 24), which accounts for
 1191 changes in isobath surface area $A(z)$ with depth but ignores correlations between w , κ , and
 1192 N^2 and excludes the horizontal advection. The solid blue lines in panels (a), (b), and (c)
 1193 show the individual components of the expressions: (a) the horizontally-averaged stratifica-
 1194 tion $\langle N^2 \rangle$, (b) the horizontally-averaged buoyancy flux $\langle \kappa \rangle \langle N^2 \rangle$, and (c) the isobath surface
 1195 area $A(z)$. The dashed line in (b) shows the role of correlation terms $\langle \kappa N^2 \rangle - \langle \kappa \rangle \langle N^2 \rangle$ in
 1196 setting the vertical structure of the buoyancy flux. Finally, the solid black line in (d) shows
 1197 the net watermass transformation, where its native density coordinate has been mapped into
 1198 a pseudo-depth coordinate by taking the average depth of a given buoyancy surface (eq. 19).
 1199 For all of our simulations, vertical advection-diffusion bulk models are poor approximations
 1200 of diapycnal abyssal upwelling. 68

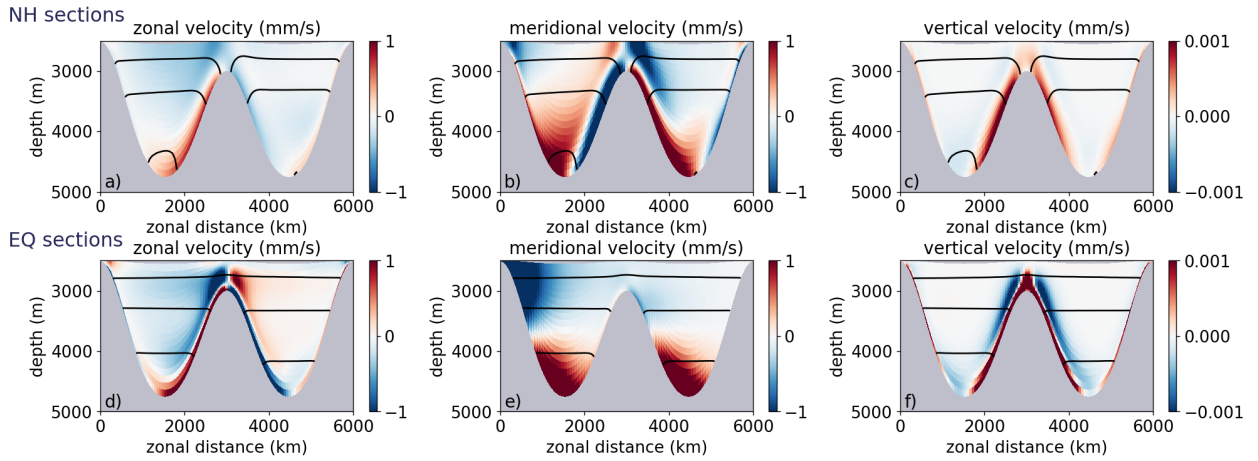
1201 **Fig. 14.** Decomposition of the watermass transformation into various physical components in the
 1202 PGCM-REAL experiment (top row) and an experiment with a shorter ridge and constant refer-
 1203 ence stratification (bottom row). In panels (a,c), we approximate the full watermass trans-
 1204 formation (dashed black) by the contribution from the vertical buoyancy flux $\partial_b (A \langle \kappa \partial_z b \rangle)$
 1205 (solid black), which we then decompose into an uncorrelated component $\partial_b (A \langle \kappa \rangle \langle \partial_z b \rangle)$
 1206 (solid blue) and a residual $\partial_b (A \langle \kappa' \partial_z b' \rangle)$ (solid orange), where $\langle \cdot \rangle$ denotes averaging along
 1207 a buoyancy surface. In panels (b,d), we further decompose the uncorrelated component into
 1208 contributions due to the buoyancy derivative of the mean stratification $\partial_b \langle \partial_z b \rangle$ (dashed) and
 1209 the integrated diffusivity along a buoyancy surface $\partial_b (A \langle \kappa \rangle)$ (dotted). 69



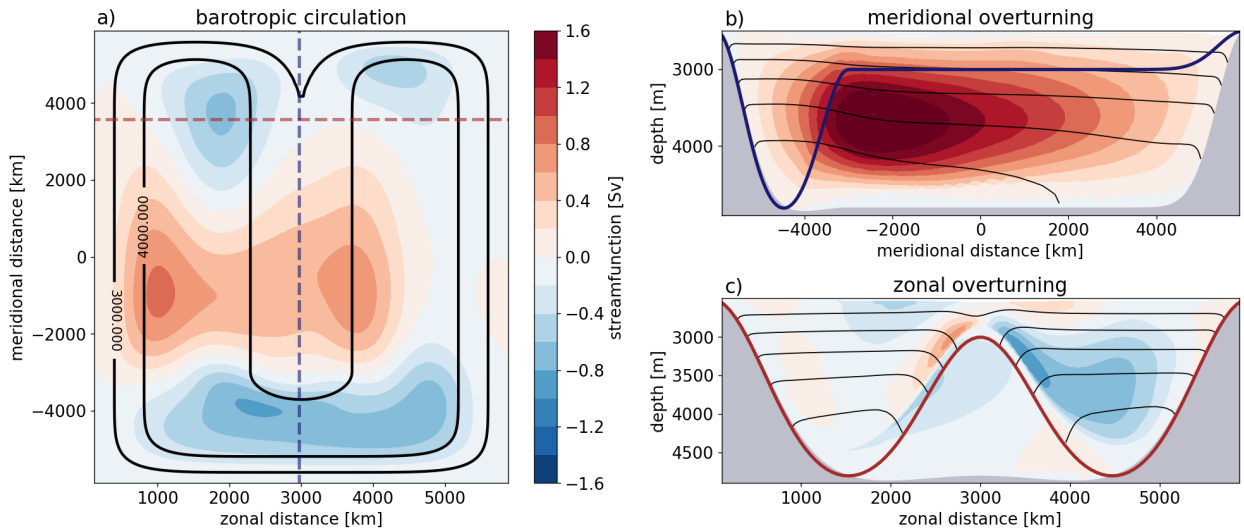
1210 FIG. 1. Schematic of a basin-scale abyssal circulation driven by near-boundary mixing. Dense bottom waters
 1211 flow northward out of the Southern Ocean via a deep western boundary current (red circle) along the smooth and
 1212 relatively quiescent continental slope, where little watermass transformation occurs. A cross-basin zonal flow
 1213 feeds bottom waters from the deep western boundary current into a system of abyssal mixing layers driven by
 1214 bottom-enhanced turbulent mixing over the rough topography of the mid-ocean ridge flanks (squiggly orange
 1215 arrows). The turbulent buoyancy flux converges in a bottom boundary layer (BBL), driving vigorous diabatic
 1216 upwelling across buoyancy surfaces (grey lines). In a stratified mixing layer (SML) above, the buoyancy flux
 1217 diverges, driving diabatic downwelling. The net effect of the up- and down-welling in the abyssal mixing layers
 1218 is a net transformation of bottom waters into deep waters. The newly formed deep waters return via cross-basin
 1219 zonal flows to the smooth continental slope, wherein they flow southward in a deep western boundary current
 1220 (blue circles) to close the abyssal circulation in the Southern Ocean. For simplicity, we omit the alternating
 1221 along-ridge flows (see Figure 3b) that are in frictional thermal-wind balance with the plunging isopycnals.



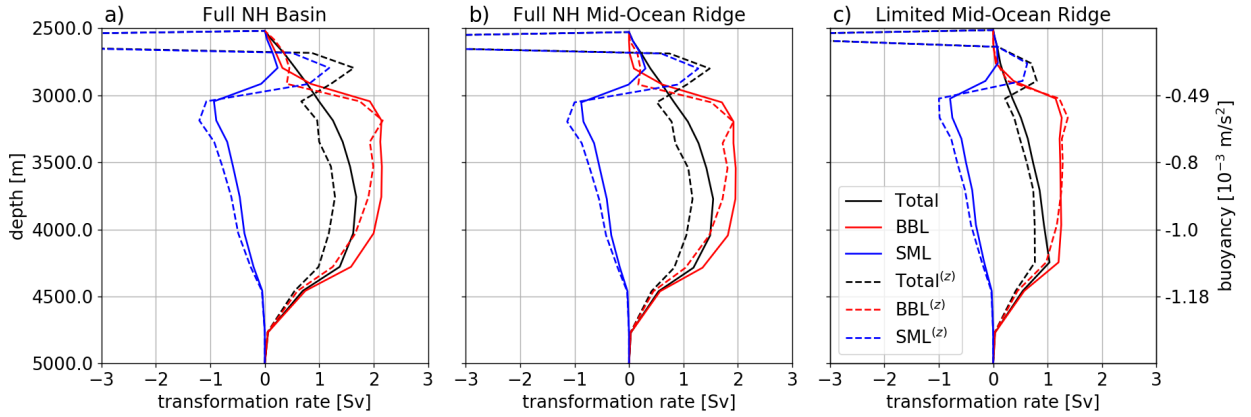
1222 FIG. 2. Configuration of the Planetary Geostrophic Circulation Model (PGCM). (a) Seafloor depth in the
 1223 PGCM. We highlight the southern restoring region where we apply a buoyancy restoring which acts to transform
 1224 deep waters into bottom waters (see Section 3c) and a northern-hemisphere region in which we diagnose wa-
 1225 termass transformations along the mid-ocean ridge (see Section 4c). (b) Zonal section of the imposed turbulent
 1226 diffusivity κ , which is bottom-enhanced over the mid-ocean ridge. (c) The red lines show the four stratification
 1227 profiles B_z used in the PGCM as both the initial condition and as the reference profile for buoyancy restoring
 1228 in the southern restoring region. The black line shows the observed stratification profile from the World Ocean
 1229 Circulation Experiment (Gouretski and Koltermann 2004) in the South Pacific, averaged horizontally from 55°S
 1230 to 45°S and 175°E to 115°W.



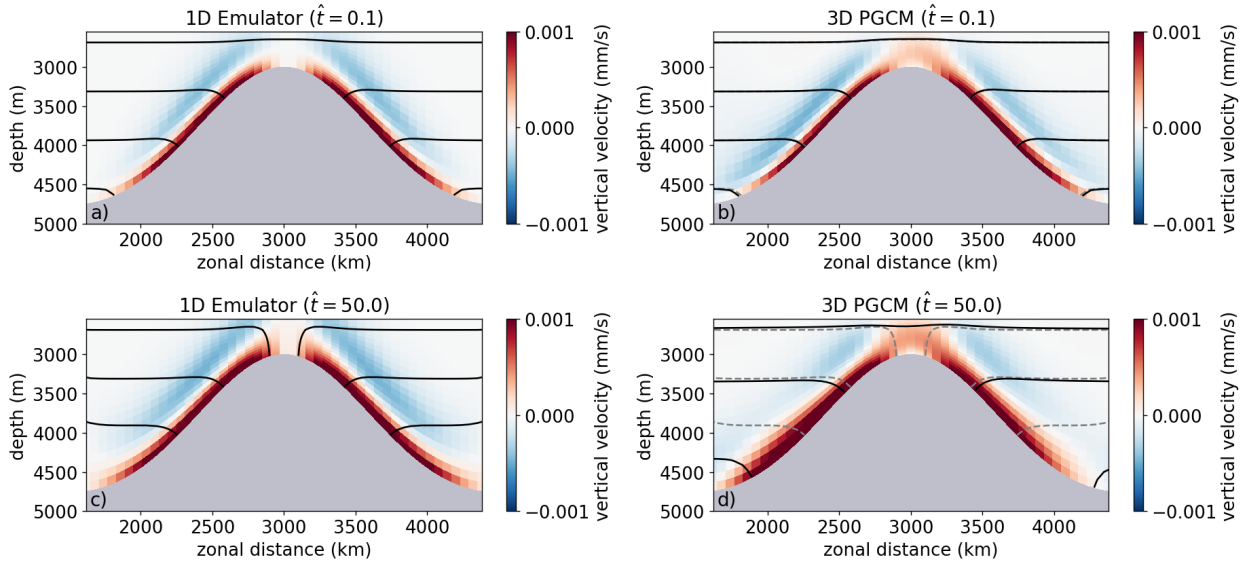
1231 FIG. 3. Cartesian components of the velocity vector in the PGCM-REAL simulation along: (a-c) a mid-
 1232 latitude section in the northern hemisphere, $y = 3000$ km, and (d-f) a section at the equator, $y = 0$ km. Black
 1233 lines show three equally spaced buoyancy surfaces.



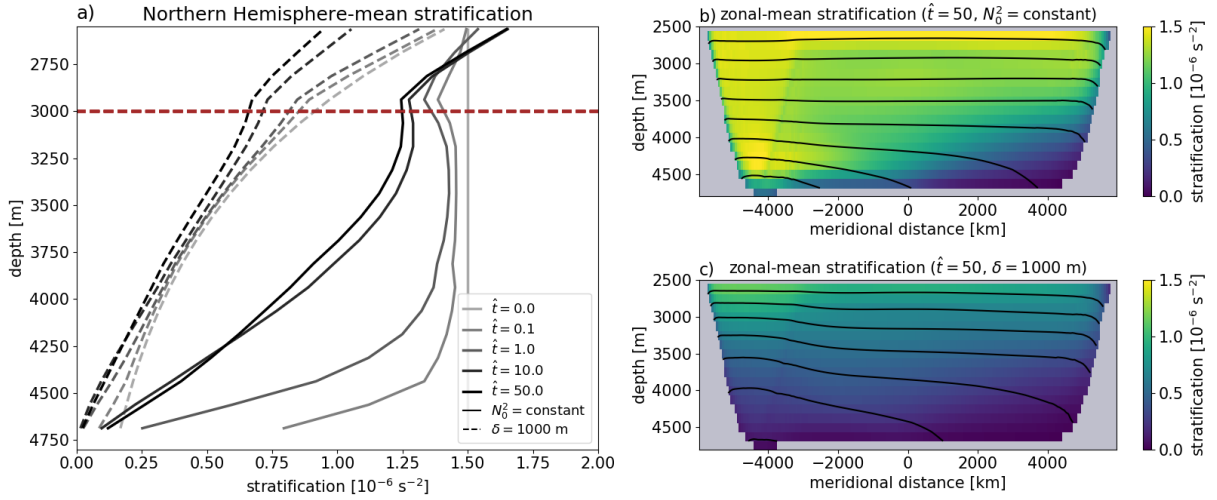
1234 FIG. 4. (a) Barotropic, (b) meridional, and (c) zonal overturning circulations in the PGCM-REAL simulation
 1235 (see definitions in Section 4b). In all cases, positive values (red) correspond to counter-clockwise circulations.
 1236 The blue and red solid lines in (b) and (c), respectively, show the height of the mid-ocean ridge along the dashed
 1237 lines of the same colors in (a). The thick black lines in (a) are the 3000 m and 4000 m isobaths, which highlight
 1238 both the continental slopes and the mid-ocean ridge. The thin black lines in (b) and (c) are equally-spaced
 1239 buoyancy surfaces, sampled at $x = L/4$ and $y = L/2$, respectively.



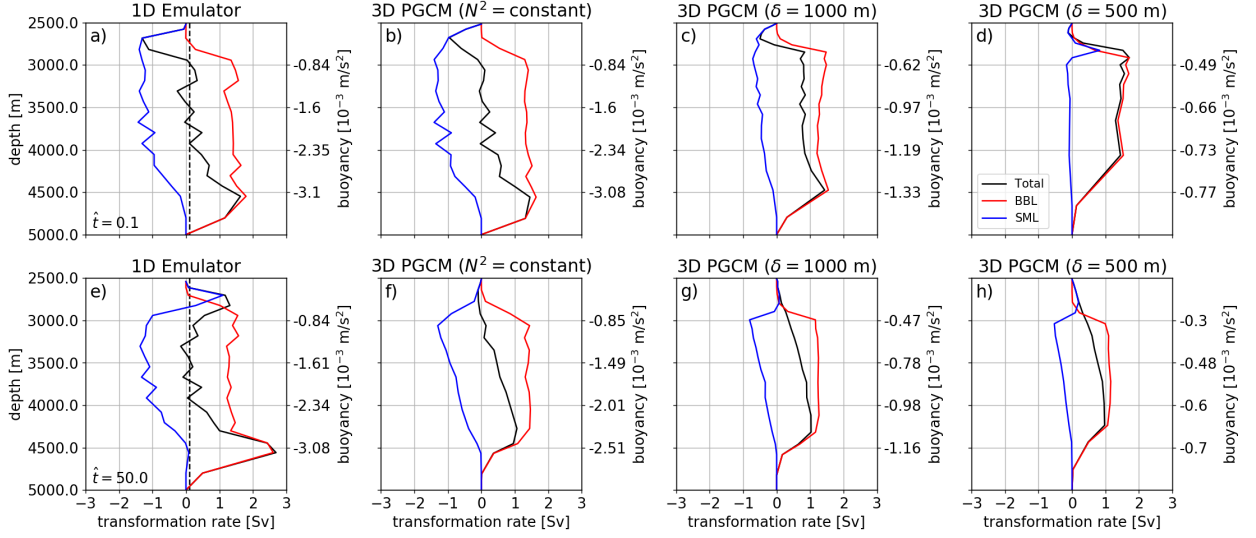
1240 FIG. 5. Watermass transformations from the PGCM-REAL simulation in (a) the full northern hemisphere
 1241 basin ($y > 0$), (b) along the northern-hemisphere mid-ocean ridge ($y > 0, L/2 < x < 3L/2$), and (c) in a limited
 1242 watermass analysis region along the northern-hemisphere mid-ocean ridge ($0 < y < L/2, L/2 < x < 3L/2$), as
 1243 highlighted in Figure 2. The black line shows the net watermass transformation, defined by equation (18). The
 1244 red and blue lines show the contributions from the bottom boundary layer (BBL) and the stratified mixing layer
 1245 above (SML). The dashed lines show the contributions from only the vertical component of the buoyancy flux.
 1246 All watermass transformations in the paper are computed in buoyancy space and remapped into depth space
 1247 (according to eq. 19).



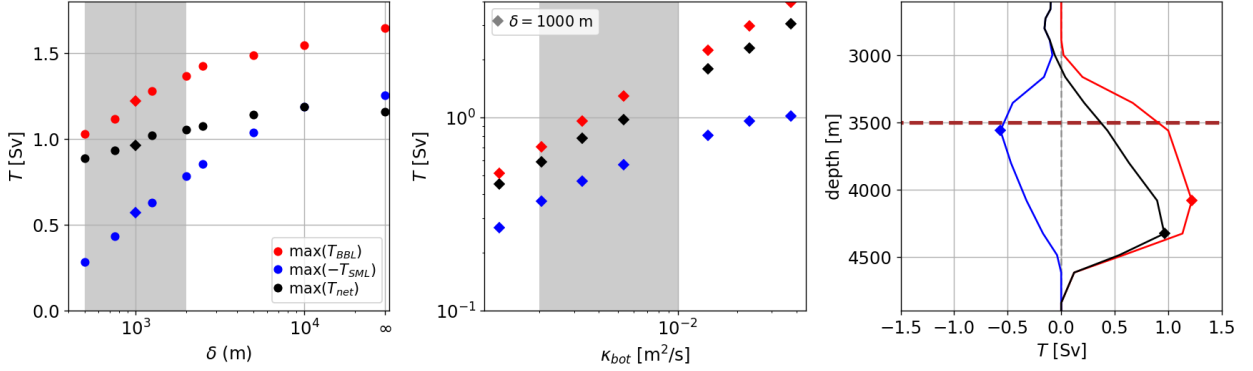
1248 FIG. 6. Vertical velocity (colors) and buoyancy surfaces (black lines) in abyssal mixing layers along a zonal
 1249 section across the mid-ocean ridge at $y = L/2$ in (a,c) the 1D PGCM emulator and (b,d) the full 3D PGCM,
 1250 where both are initialized from identical constant stratification buoyancy fields. The top row shows the solutions
 1251 at an initial time $\hat{t} = 0.1$, at which point the abyssal mixing layers have spun up but the basin-scale circulation has
 1252 not (see Section 3d). The bottom row shows the solution at $\hat{t} = 50$, at which point the full solution has roughly
 1253 come to equilibrium with the buoyancy restoring in the Southern Ocean. The predicted buoyancy surfaces in
 1254 (a,c) are reproduced as dashed grey lines in (b,d) to show how the 1D emulator predicts the buoyancy field well
 1255 for short times but that the interior stratification in the PGCM drifts far from the 1D emulator's prediction as it
 1256 approaches equilibrium.



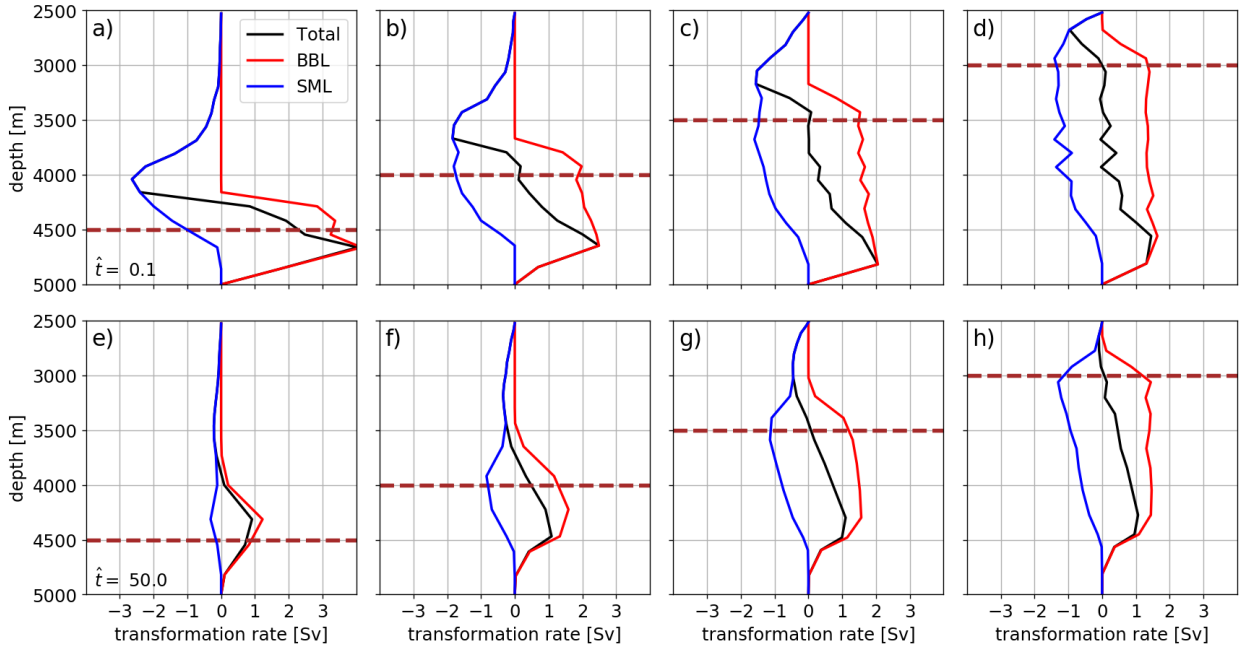
1257 FIG. 7. (a) Temporal evolution and (b,c) meridional structure of the stratification in PGCM simulations. Grey-
 1258 scale lines in (a) show the temporal evolution of the horizontal-mean stratification in the Northern Hemisphere
 1259 for simulations with a constant stratification restoring buoyancy profile (solid lines) and a restoring buoyancy
 1260 profile corresponding to stratification that decays with depth with a scale height of $\delta = 1000$ m (dashed lines).
 1261 The dashed brown line delineates the height of the ridge crest. Panels (b) and (c) show the zonal-mean stratifi-
 1262 cation at equilibrium $\hat{t} = 50$ (colors) and equally-spaced buoyancy surfaces (black lines) for experiments with
 1263 restoring to constant and exponential stratification, respectively.



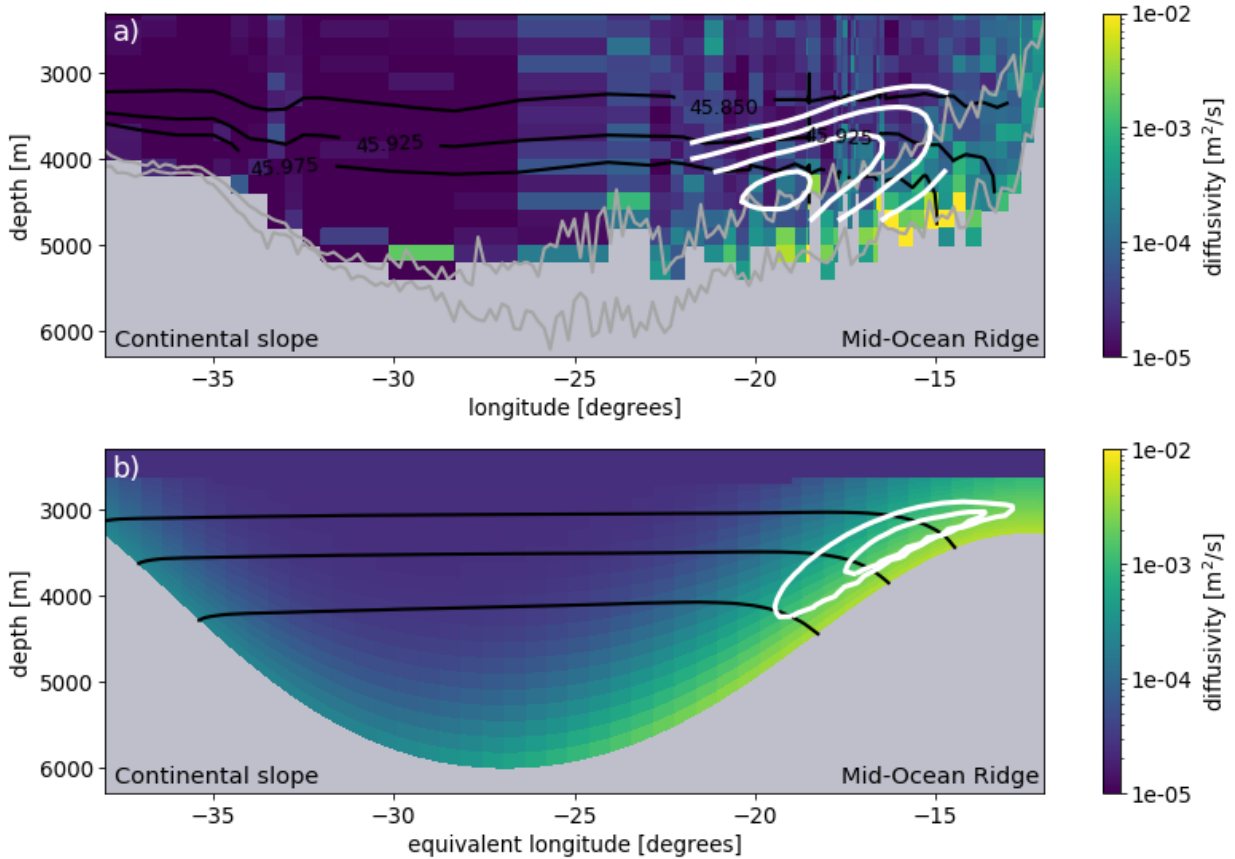
1264 FIG. 8. Watermass transformations in: (a, e) a 1D emulator of the PGCM and (b-d, f-h) the 3D PGCM
 1265 simulations with restoring buoyancy profiles corresponding to stratification profiles with various exponential
 1266 scale heights δ (we recover $N^2 = \text{constant}$ as $\delta \rightarrow \infty$). The initial spin-up at $\hat{t} = 0.1$ is shown in (a-d) and the
 1267 equilibrium state at $\hat{t} = 50$ is shown in (e-h). Black, red, and blue lines show the net, bottom boundary layer
 1268 (BBL), and stratified mixing layer (SML) contributions to the watermass transformations, respectively. The
 1269 black dashed line in (a,e) shows the integral constraint $L\Psi_\infty = L\kappa_{\text{bg}} \cot \theta_{\text{max}}$ derived from boundary layer theory,
 1270 where we take θ_{max} as the maximum slope angle of the mid-ocean ridge flank.



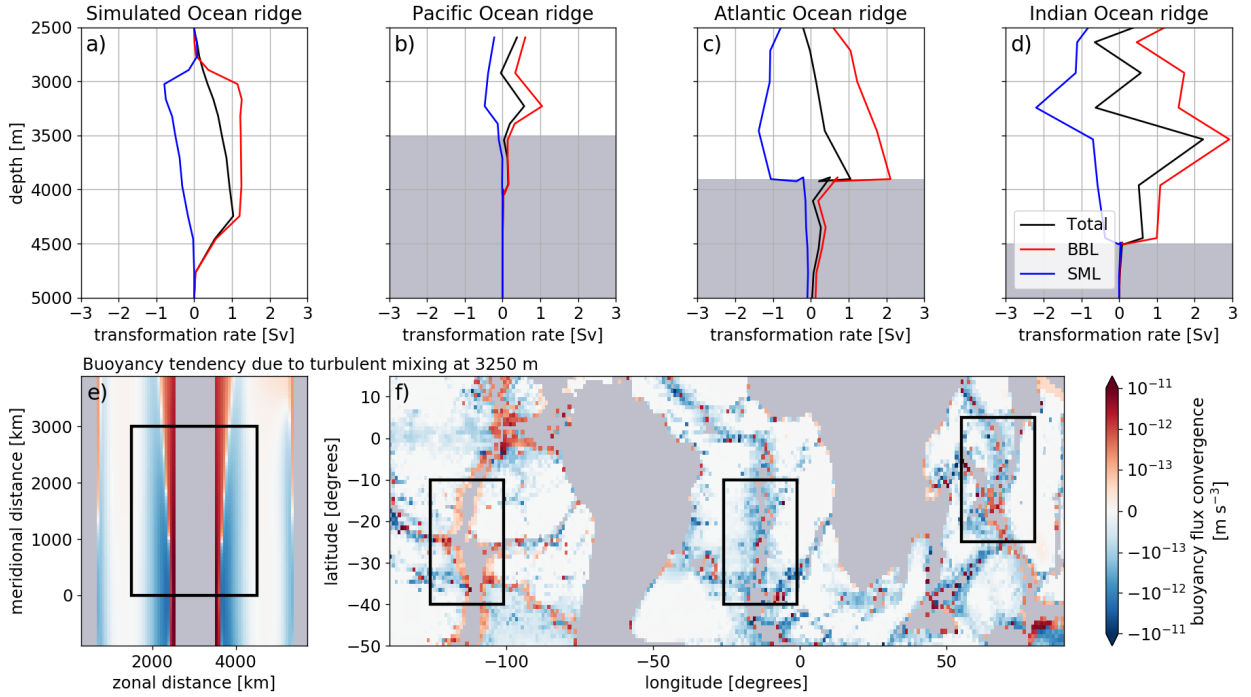
1271 FIG. 9. Scaling of watermass transformations in mixing layers with (a) the height δ over which the restoring
 1272 stratification varies and (b) the bottom diffusivity κ_{bot} . Colored symbols represent the absolute value of the
 1273 maximum transport in the BBL (red), the SML (blue), and the net (black), with diamonds representing the
 1274 PGCM-REAL simulations. The grey shading in (a) represents realistic vertical scales δ over which abyssal
 1275 stratification varies and in (b) represents plausible values of the bottom diffusivity κ_{bot} . Panel (c) provides
 1276 an example of the watermass transformations for a bottom diffusivity $\kappa_{bot} = 5 \times 10^{-3} \text{ m}^2\text{s}^{-1}$, a stratification
 1277 height scale $\delta = 1000 \text{ m}$, and a ridge height of $r_h = 1500 \text{ m}$, where the corresponding maxima are marked by
 1278 diamonds and the dashed brown line represents the ridge crest. In all experiments, the maximum net and BBL
 1279 transformations occur at depths of roughly 4250 m, at the base of the ridge slope, while the maximum SML
 1280 transformation occurs at the ridge crest.



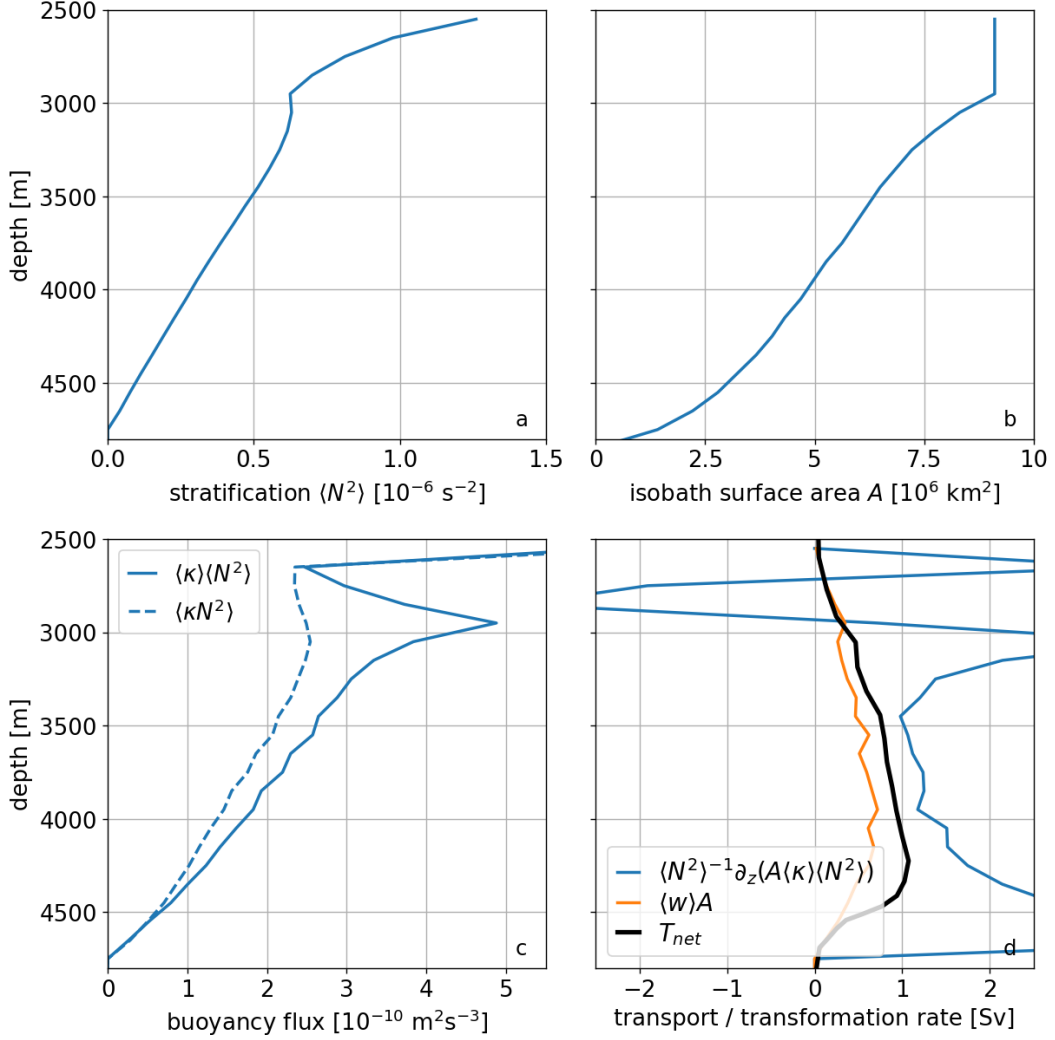
1281 FIG. 10. Watermass transformations in PGCM simulations as a function of ridge height. All panels are for a
 1282 fixed constant stratification restoring buoyancy profile. The initial spin-up at $\hat{t} = 0.1$ is shown in (a-d) and the
 1283 equilibrium state at $\hat{t} = 50$ is shown in (e-h). Mid-ocean ridge height increases in increments of 500 m from left
 1284 to right, as indicated by the dashed brown lines. Black, red, and blue lines show the net, bottom boundary layer
 1285 (BBL), and stratified mixing layer (SML) contributions to the watermass transformations, respectively.



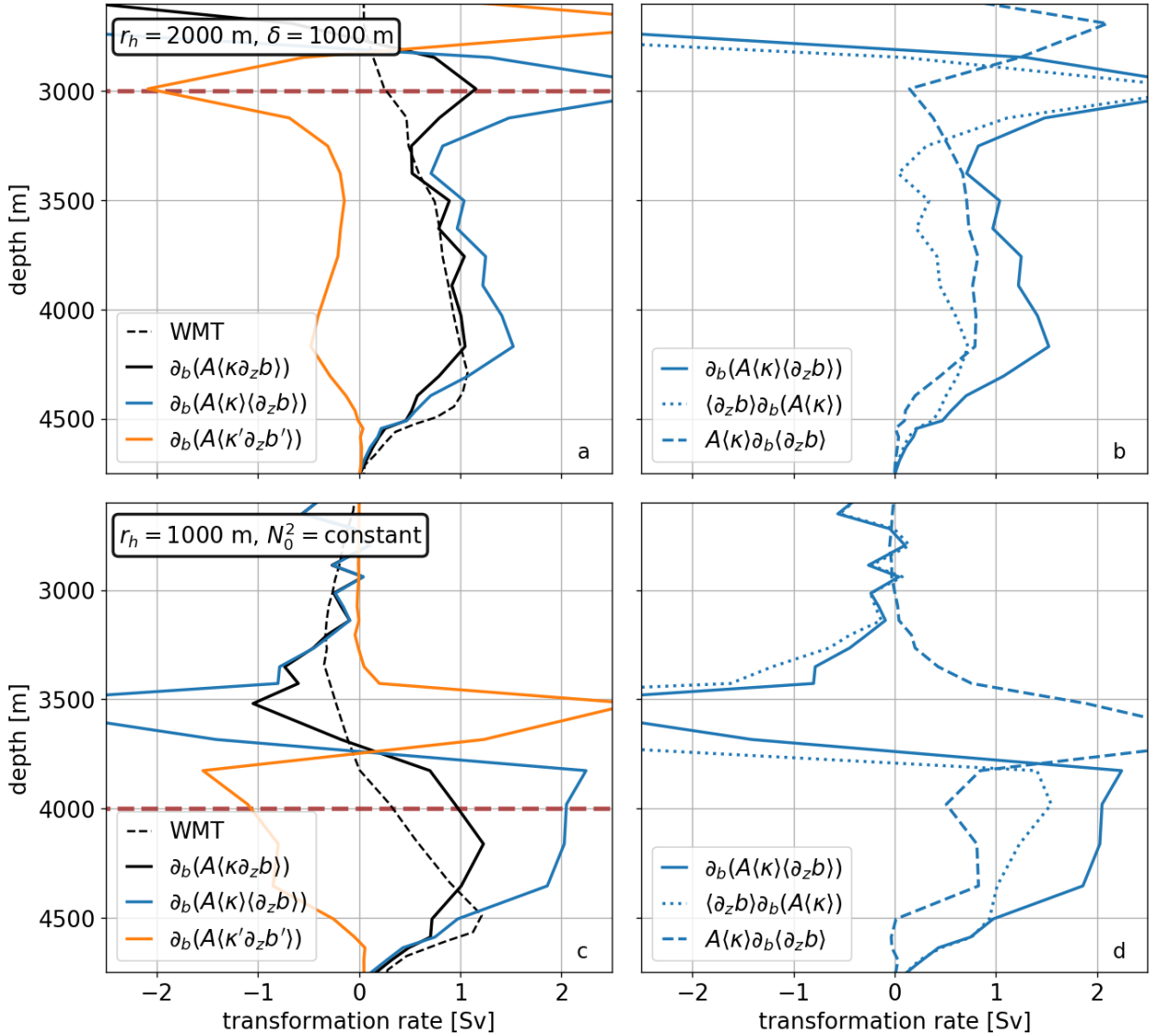
1286 FIG. 11. Diabatic zonal overturning circulation driven by bottom-enhanced mixing on the western flank
 1287 of a mid-ocean ridge in (a) the South Atlantic Ocean and (b) the western half of the PGCM-REAL simulation
 1288 domain. White lines show arbitrarily chosen contours of the counter-clockwise zonal overturning streamfunction,
 1289 where the values for (a) are digitized from Figure 14 of St. Laurent et al. (2001) and for (b) are diagnosed from
 1290 PGCM-REAL simulation. Coloring shows the vertical diffusivity in log-scale (light-grey shading represents
 1291 depths with no microstructure measurements and does not necessarily represent topography), where panel (a) is
 1292 inspired by Figure 2 of Polzin et al. (1997) and the diffusivity is calculated with microstructure profiles from the
 1293 BBTRE experiment (Polzin et al. 1997; St. Laurent et al. 2001, archived at microstructure.ucsd.edu). Black lines
 1294 are: (a) potential density σ_4 surfaces (referenced to 4000 m) from the microstructure profiles and (b) buoyancy
 1295 surfaces from the PGCM solution, chosen arbitrarily to show that the zonal overturning circulation is indeed
 1296 diabatic. The dark grey lines in (a) show the depth minimum (canyon thalweg) and maximum (canyon crest)
 1297 seafloor depth within 0.5° latitude of the microstructure profiles. In (b), zonal distance along the PGCM section
 1298 has been converted to an equivalent longitude at 25° S so that length scales can be directly compared between
 1299 the two panels.



1300 FIG. 12. (a-d) Watermass transformations at all abyssal depths and (e,f) buoyancy flux convergence at 3250 m
 1301 depth in similarly-sized domains containing mid-ocean ridges, as diagnosed from (a,e) the PGCM-REAL simu-
 1302 lation and estimated for the (b,f) Pacific, (c,f) Atlantic, and (d,f) Indian Oceans. In (a-d), the black, red, and blue
 1303 lines show the net, bottom boundary layer (BBL), and stratified mixing layer (SML) contributions to the wa-
 1304 termass transformations, respectively (grey shaded indicates depths representing very little ocean volume). The
 1305 black boxes in (e,f) delineate the similarly-sized regions (each with dimensions of roughly $3000 \text{ km} \times 3000 \text{ km}$)
 1306 for which we compute the watermass transformations. In (e,f), red and blue show regions of buoyancy flux
 1307 convergence (positive buoyancy tendency) and buoyancy flux divergence (negative buoyancy tendency), respec-
 1308 tively.



1309 FIG. 13. Comparison of abyssal upwelling diagnostics in the PGCM-REAL simulation for the water-
 1310 mass transformation analysis region highlighted in Figure 2a. The orange and blue lines in panel (d) rep-
 1311 resent the left- and right-hand sides, respectively, of the horizontally-averaged advection-diffusion balance
 1312 $\langle w \rangle A \simeq \langle N^2 \rangle^{-1} \frac{d}{dz} [A(z) \langle \kappa \rangle \langle N^2 \rangle]$ (eq. 24), which accounts for changes in isobath surface area $A(z)$
 1313 but ignores correlations between w , κ , and N^2 and excludes the horizontal advection. The solid blue lines in
 1314 panels (a), (b), and (c) show the individual components of the expressions: (a) the horizontally-averaged strat-
 1315 ification $\langle N^2 \rangle$, (b) the horizontally-averaged buoyancy flux $\langle \kappa \rangle \langle N^2 \rangle$, and (c) the isobath surface area $A(z)$. The
 1316 dashed line in (b) shows the role of correlation terms $\langle \kappa N^2 \rangle - \langle \kappa \rangle \langle N^2 \rangle$ in setting the vertical structure of the
 1317 buoyancy flux. Finally, the solid black line in (d) shows the net watermass transformation, where its native den-
 1318 sity coordinate has been mapped into a pseudo-depth coordinate by taking the average depth of a given buoyancy
 1319 surface (eq. 19). For all of our simulations, vertical advection-diffusion bulk models are poor approximations of
 1320 diapycnal abyssal upwelling.



1321 FIG. 14. Decomposition of the watermass transformation into various physical components in the PGCM-
 1322 REAL experiment (top row) and an experiment with a shorter ridge and constant reference stratification (bottom
 1323 row). In panels (a,c), we approximate the full watermass transformation (dashed black) by the contribution
 1324 from the vertical buoyancy flux $\partial_b(A\langle\kappa\partial_z b\rangle)$ (solid black), which we then decompose into an uncorrelated
 1325 component $\partial_b(A\langle\kappa\rangle\langle\partial_z b\rangle)$ (solid blue) and a residual $\partial_b(A\langle\kappa'\partial_z b'\rangle)$ (solid orange), where $\langle\cdot\rangle$ denotes averaging
 1326 along a buoyancy surface. In panels (b,d), we further decompose the uncorrelated component into contributions
 1327 due to the buoyancy derivative of the mean stratification $\partial_b\langle\partial_z b\rangle$ (dashed) and the integrated diffusivity along a
 1328 buoyancy surface $\partial_b(A\langle\kappa\rangle)$ (dotted).